UNIVERSITÀ DEGLI STUDI DI PADOVA

UNIVERSITA' DEGLI STUDI DI PADOVA

Dipartimento di Ingegneria Industriale DII

Dipartimento di Scienze Chimiche

Corso di Laurea Magistrale in Ingegneria dei Materiali

Bifunctional dual-atom catalysts for Oxygen Electrode Reactions in Metal-air batteries

Relatore: Prof. Laura Calvillo Lamana

Laureando: Giovanni Zava 2054473

Anno Accademico 2023/2024

Abstract

The increasing energy demand and the pressing climate change are recently motivating the conversion of the energy supply chain from fossil fuels to renewable sources. These systems, however, are limited by their intermittence in energy production. This fact poses the challenge of finding new effective ways to store energy. Electrochemical storage systems are one of the most promising solutions to this issue. Among them, secondary metal-air batteries are elected as a key candidate due to their security, scalability, affordability, and intrinsic specific energy.

The performances of these systems rely on oxygen electrode reaction since oxygen evolution reaction (OER) and oxygen reduction reaction (ORR) occur respectively in the charge and discharge of the cell. To try to facilitate the well-known sluggish kinetics of these reactions and to limit the overpotential-related energy losses in the charging and discharging process, new kinds of bifunctional catalysts are being developed. Among them, single-atom catalysts and dual-atom catalysts, made by single metal atoms well-coordinated in a conductive support, seem to be the most promising to replace the well-performing, though scarce and expensive, noble metals such as platinum, iridium, and rhodium.

In this thesis, the electrochemical activity towards oxygen electrode reactions of single and dual-atom catalysts based on iron and manganese on a nitrogen-doped carbon nanotube support was investigated. The tested catalysts were obtained through a thermal synthesis and characterized using transmission electron microscopy (TEM), X-ray Diffraction (XRD), and X-ray Photoelectron Spectroscopy (XPS). The electrochemical performance of the proposed catalysts was determined by evaluating the ORR and OER activity in alkaline electrolyte using rotating disk electrode (RDE) and rotating-ring disk electrode (RRDE). The effect of the iron-to-manganese ratio on the morphology and the activity of the synthesized materials was also examined.

Sommario

La crescente domanda di energia e l'urgente necessità di contrastare il cambiamento climatico stanno accelerando la transizione dai combustibili fossili alle fonti energetiche rinnovabili. Tuttavia, l'intermittenza nella produzione di energia da questi sistemi rappresenta una sfida per lo stoccaggio efficiente dell'energia. I sistemi di accumulo elettrochimico si propongono come una soluzione promettente e, tra questi, le batterie secondarie metallo-aria si distinguono per la loro sicurezza, scalabilità, economicità ed elevata densità di energia.

Le prestazioni di queste batterie dipendono dalle reazioni all'elettrodo di ossigeno: la reazione di evoluzione dell'ossigeno (OER) durante la carica e la reazione di riduzione dell'ossigeno (ORR) durante la scarica. Per superare la cinetica lenta di queste reazioni e minimizzare le perdite di energia legate al sovra potenziale durante la carica e la scarica, sono in fase di sviluppo nuovi catalizzatori bifunzionali. I catalizzatori a singolo atomo e a doppio atomo, composti da singoli atomi metallici ancorati a un supporto conduttivo, appaiono come i sostituti più promettenti per i metalli nobili, ad alte prestazioni ma rari e costosi, come platino, iridio e rodio.

In questa tesi sono è stata investigata l'attività elettrochimica per le reazioni all'elettrodo di ossigeno di catalizzatori a singolo e doppio atomo basati su ferro e manganese su supporti di nanotubi di carbonio dopati con azoto. I catalizzatori sono stati sintetizzati termicamente e caratterizzati mediante microscopia elettronica a trasmissione (TEM), diffrazione di raggi X (XRD) e spettroscopia fotoelettronica a raggi X (XPS). Le loro prestazioni elettrochimiche per ORR e OER sono state valutate in elettrolita alcalino mediante elettrodo a disco rotante (RDE) ed elettrodo a disco ad anello rotante (RRDE). Infine, è stata esaminata l'influenza del rapporto ferro-manganese sulla morfologia e sull'attività dei materiali sintetizzati.

Index

CHAPTER 1 – INTRODUCTION

1.1 – Energy

In today's world, we are confronted with a crucial energy dilemma that calls for urgent action. We must address the challenge of mitigating climate change while also meeting the growing energy demand, without compromising human development. This complex energy problem stems from factors such as our reliance on fossil fuels, inefficient energy systems, and the need to shift towards renewable sources. **Figure 1** reports the outstanding increase in energy demand forecast for 2030 both on the global and per-capita levels. Given the current energy production systems, based primarily on fossil fuels, an increase in energy demand is to be associated with an increase in greenhouse gases and CO_2 emissions, aggravating the yet problematic climate change.

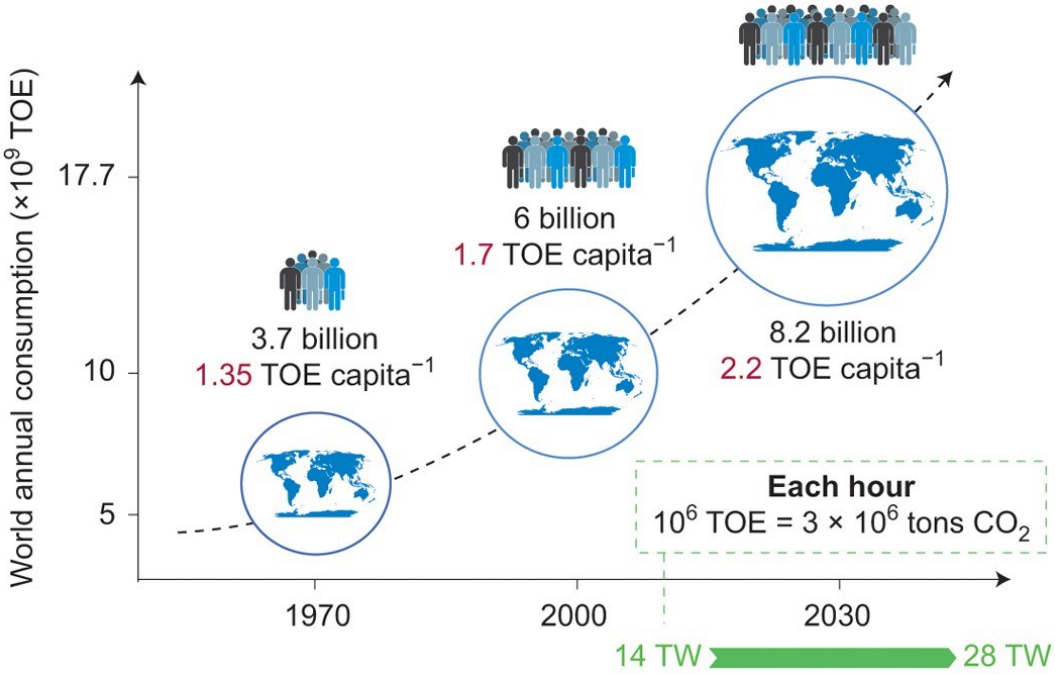

Figure 1. *Past, present, and forecast of the world's energy needs up to 2050 adapted from ref. [1] (TOE = ton of oil equivalent)*

In recent years, the focus on sustainable development has occupied a relevant position in the social, mediatic, governmental, and scientific spheres, reflecting a growing awareness of the urgent need for collective action to address the issue. As outlined in the *Net Zero Scenario* by the International Energy Agency (*IEA*), achieving carbon neutrality by 2050 is not only of paramount importance but an existential necessity to safeguard against disastrous climate impacts and ensure a sustainable future for all.

One of the main focuses of the IEA report is electricity. IEA data report an increase in electricity production of 84% between 2000 and 2021, and an additional increase of 3.6% on an annual basis

is forecasted through 2026 [2] with a predictable consistent trend in future years. Nonetheless, the possibility of rebuilding electricity generation to be progressively cleaner motivates the electrification of many sectors previously dominated by fossil fuels. Such a shift is made possible by the diffusion of renewable energy technologies that ensure sustainable and green energy production.

1.2 – Renewable Energy Sources

Renewable electricity generation is one of the key parameters presented in the latest IEA global guideline for sustainable development: the Net Zero Emissions by 2050 Scenario (*NZE Scenario*). It consists of a pathway for the global energy sector to achieve net zero CO_2 emissions by 2050, limiting the global temperature rise to 1.5 C (with at least a 50% probability), in line with emissions reductions assessed in the Intergovernmental Panel on Climate Change (IPCC)'s Sixth Assessment Report. The NZE scenario accounts for the renewable electric grid to triple by 2030 and to grow eightfold by 2050, as shown in **Figure 2**.

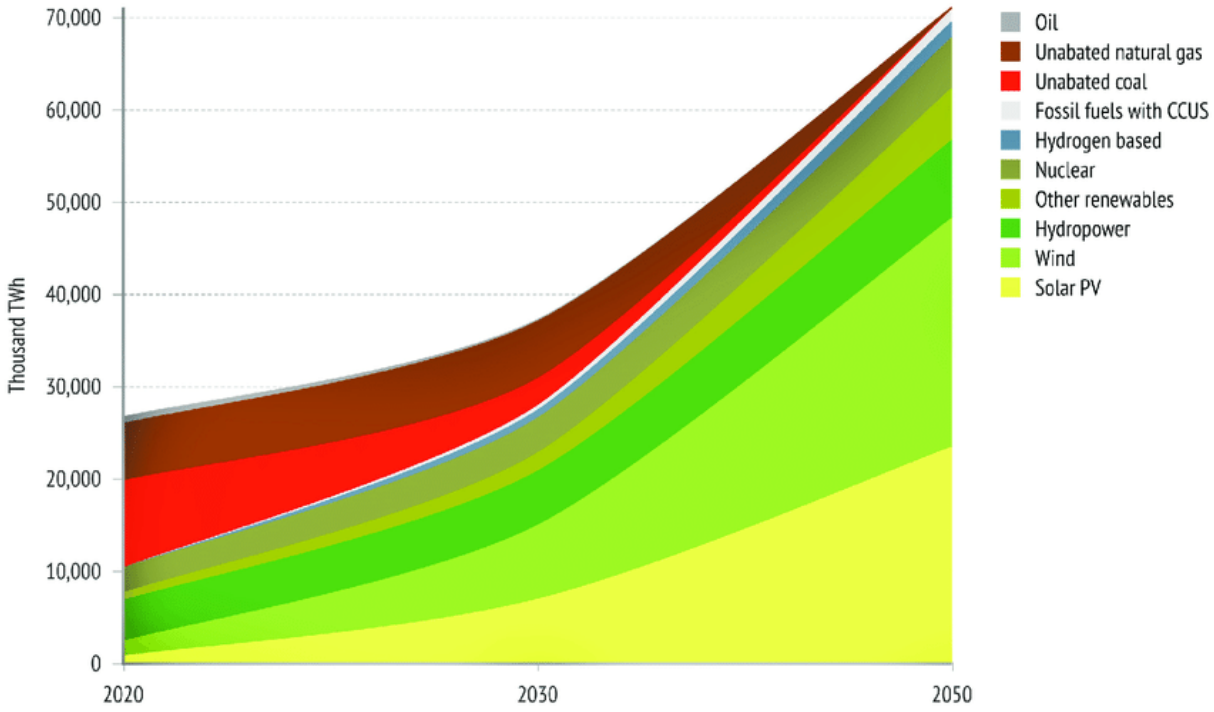

Figure 2. *Global electricity generation forecast by source in the Net Zero by 2050 scenario adapted from ref. [3]*

Considering the forecasted energy mix, the fraction of electricity generated from solar photovoltaic, and wind will reach the value of 67% by 2050. These technologies are however intermittent, depending on the local and variable climatic conditions, exposing the whole electricity distribution system to fluctuations and energy shortages.

1.3 – Energy storage

The ever-growing energy demand together with the fluctuations of green energy sources motivates the interest in energy storage technologies. Energy storage systems allow for balancing the unstable load impacts of renewable energies, offering extra services such as frequency and voltage stability, maintaining a stable energy supply, and increasing dependability and spread [4]. In general, such systems can be categorized into five groups according to how energy is effectively stored: mechanical, thermal, chemical, electrical, and electrochemical storage. *Mechanical* storage systems rely on converting the energy source into mechanical energy, either kinetic or potential. The most diffused technologies are pumped storage hydropower, compressed air storage, and flywheels. *Thermal* storage systems exploit the energy source to accumulate sensible or latent heat or to promote high-temperature thermochemical reactions. In *Chemical* storage systems the energy provided by the source is accumulated in the chemical bonds of a fuel, commonly molecular hydrogen, hydrocarbons, and ammonia. Double-layer capacitors are the most diffused technology concerning *electrical* energy storage. In these devices, energy can be stored as charges on the surface of the electrodes. Finally, *electrochemical* energy storage systems convert the supplied electrical energy into chemical energy that is stored thanks to a redox reaction.

Having such a wide range of different technologies on whom they rely, energy storage systems show very different operational parameters and performance. In particular, their goodness and suitability for wide diffusion should be evaluated considering initial investment, discharge time, reaction time response, rated power, efficiency, stability in time, and expected lifetime.

As a result of their inherent characteristics, thermal energy storage devices are to be excluded from the competition since they are characterized by time-limited storage and extremely poor efficiency of the reverse recovery of heat into electricity. Electrical systems instead are yet to achieve sufficient rated power to provide widespread diffusion. As represented in **Figure 3**, the best results in terms of discharge time and rated power are characteristic of pumped storage hydroelectric systems. Despite their performance and the associated low operational cost, such systems are limited by site selection and require a large initial investment and long construction periods as well as a long reaction time (up to 10 min) [5].

One of the most promising technologies for storing excess energy from renewable systems during off-peak hours is the production and storage of hydrogen. These storage technologies present a power rate range in the order of 10 MW and are suitable for long-term storage [6]. However, the commercialization of Hydrogen-based systems requires addressing challenges related to storage methods, transportation modes, efficiency optimization, and technology adoptions [7].

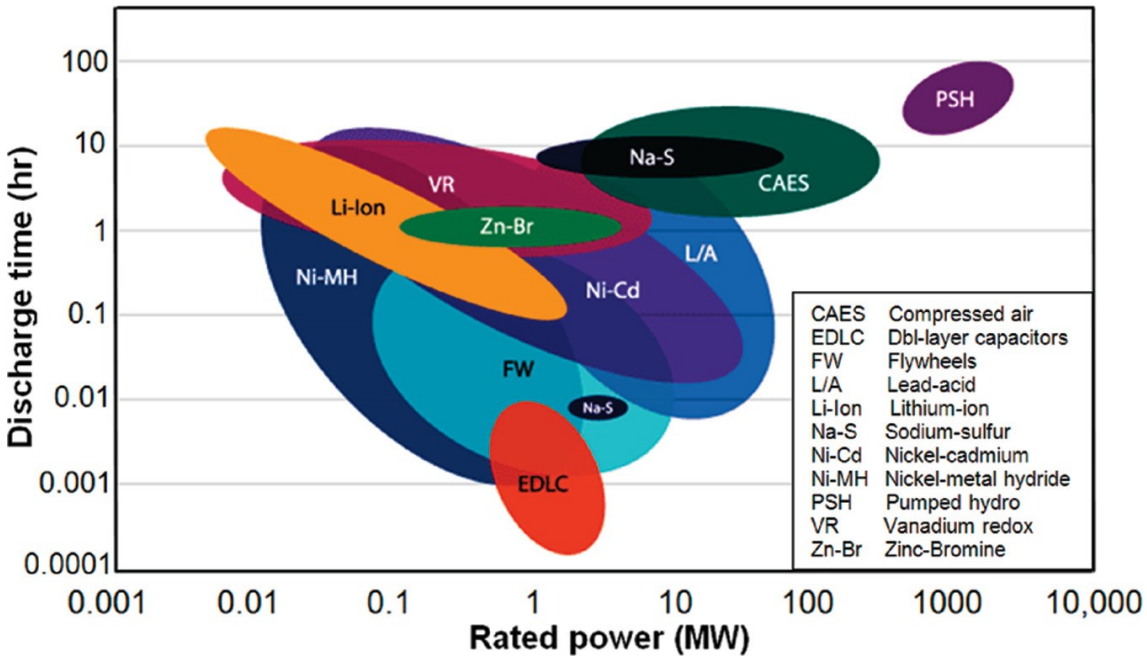

Figure 3. *Power ratings and discharge times (i.e., energy ratings) of varied technologies adapted from ref. [5]*

Electrochemical storage systems instead, showing intermediate performances among the available technologies fast reaction time, and good reliability are elected to be the leading energy storage solution.

Among the several electrochemical technologies, Lithium-ion batteries are regarded as the most viable options for grid-scale energy storage. However, current lithium-ion technology is still suffering from insufficient energy density, relatively high cost, and potential safety risks [8]. Lithium-ion technology is also limited by the provision of raw materials involved in its manufacturing. In fact, several of its key components have been consistently listed among the Critical Raw Materials by the European Commission, being subject to potential supply risk in the future. Cobalt and Graphite have belonged to this list since 2010 while Lithium has been present since 2020. These materials are massively employed to realize the electrodes in Li-ion batteries but other key elements, such as the Copper electrical contacts or the Fluorine-based electrolytes, are also depicted in the list.

The issue of the limited reservoir of these materials grows worse if the forecast of battery demand is to be considered. According to the IEA, the *Global installed grid-scale battery storage capacity in*

the Net Zero Scenario will require 967 GW battery storage capacity in 2030. The installed value in 2022 was limited to 28 GW.

In such a framework, it is critical to find valid alternatives to Li-ion batteries to satisfy the foreseen storage demand while achieving sustainable development in terms of environmental and social impact.

1.4 – Metal-Air batteries

One of the most promising technologies is Metal-Air batteries. This category of electrochemical cells was first designed in the 1930s as primary batteries and generates electrical energy through the reaction of a metal electrode with Oxygen from the air. They are composed of a reactive metal (such as zinc, aluminum, sodium, or lithium) as the anode and an air-exposed cathode that reacts with atmospheric oxygen. The theoretical values of the cell potential, specific energy, and specific capacity depend on the choice of the metal at the anode as shown in **Table 1**.

Table 1. Comparison of four kinds of Metal Air batteries adapted from ref. [9]

Anode	**Theoretical cell voltage** *V*	**Theoretical specific energy excluding O_2** *W h kg^{-1}*	**Theoretical specific energy including O_2** *W h kg^{-1}*	**Practical specific energy** *W h kg^{-1}*
Li	3.10	11680	3500	2000
Mg	3.09	6800	3910	700
Al	2.71	8135	2800	400
Zn	1.65	1300	1086	200

Current research continues to be focused on material development to overcome the lifespan limits of these systems and cell engineering to enhance the effectiveness of the system [10].

Metal-air technology is already present in commercial products as primary Zinc-Air batteries. This kind of cell is commonly manufactured as button cells and employed in portable devices that require long-lasting power with small current drainage. Given their existing prevalence and inherent performance, this thesis will focus on Zinc-Air batteries.

Primary Zinc-Air cells show high energy density, constant output voltage (between 1.1 and 1.25 volts throughout the discharge life of the cell), excellent shelf life, intrinsic safety, and low operating cost. The operating temperatures are between 0 °C and 50 °C.

The cell electrochemical reaction is composed of an anodic and a cathodic semi-reactions, each one with its standard reduction potential E^0.

At the anode, zinc is oxidized to form zinc hydroxide in the form of the soluble zincate ion.

$$Zn + 4\ OH^- \rightarrow Zn(OH)_4{}^{2-} + 2e^- \qquad E^0 = -1.25\ V\ vs\ SHE$$

The zinc hydroxide accumulates around the zinc particle but does not impede either ionic or particle-to-particle conductance until the zinc is fully oxidized.

As the discharge proceeds, the zincate ions eventually precipitate to form zinc oxide.

$$Zn(OH)_4{}^{2-} \rightarrow ZnO + H_2O + 2\ OH^-$$

At the cathode, atmospheric oxygen is reduced to hydroxide ions with the help of a catalyst.

$$\frac{1}{2}O_2 + H_2O + 2e^- \rightarrow 2\ OH^- \qquad E^0 = 0.40\ V\ vs\ SHE$$

The whole cell reaction could be represented as

$$Zn + \frac{1}{2}O_2 \rightarrow ZnO$$

and has a standard potential of

$$E^0_{Cell} = E^0_{Cathode} - E^0_{Anode} = 1.65\ V\ vs\ SHE$$

The structure of Zn-Air batteries may be generalized as being composed of the following elements: (i) a negative pole connected to the cell anode; (ii) a positive pole electrically connected to the cathode side; (iii) a separator placed between the two electrodes; (iv) an electrolyte that ensures the ionic conductivity between the electrodes; and (v) a gasket, installed to prevent electrolyte leakage, all placed in a steel can, that presents one or more holes to allow the diffusion of atmospheric Oxygen to the cathodic site.

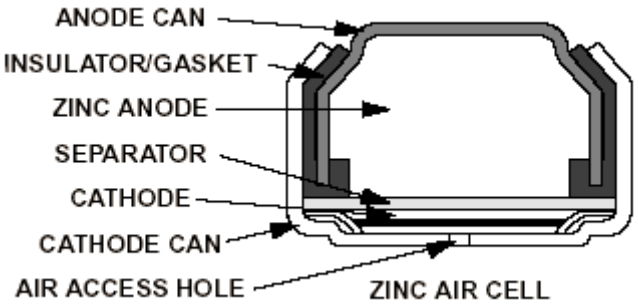

Figure 4. *Structure of a primary Zinc-Air button cell*

In commercial products, the anode is typically composed of a powdered zinc amalgam, with a very low mercury level to prevent internal pressure buildup due to hydrogen evolution. Commercial air cathodes are made of a mixture of carbon, Teflon, and a small amount of manganese dioxide impressed onto a nickel-plated screen. This material is then coupled with a Teflon layer on one side and a separating membrane on the other. The Teflon layer allows gases, most importantly oxygen, to diffuse into and out of the cell, and provides resistance to leakage. The separator acts as an ionic conductor between the electrodes and as an insulator to prevent internal short-circuiting. Being the anode-cathode voltage difference limited, the electrolyte is a conductive aqueous solution containing potassium hydroxide (KOH) with a small amount of zinc oxide to prevent self-discharge of the anode. Finally, a plastic seal is placed on top of the cell to avoid self-discharge during shelf-life.

Recently, the interest in Metal-Air batteries has been renewed by the possibility of making such devices secondary batteries and thus being rechargeable.

This result could be achieved with two different approaches, depending on the properties of the metallic anode. If the metal is prone to passivation, the active anodic sites are reduced, and the oxidation of the metal is irreversible. This behavior is typical of Mg and Al but is also considered to be the main cause of efficiency losses in Zn-Air cells after numerous cycles. In this case, the re-charging of the battery could be obtained by mechanically substituting the metallic anode with a non-passivated equivalent. If instead the effect of passivation can be neglected, the cell can be recharged without introducing any structural modification but simply ensuring that the anodic and cathodic semi-reactions are reversible. Applying then a sufficient voltage difference allows to invert the semi-reactions at each electrode. On the cathode side, the oxygen is evolved and released in the atmosphere whereas on the anode side, the metal oxide layer on the negative pole is depleted in favor of the unoxidized metal.

Considering a secondary Zinc-Air, the overall reaction cell becomes

$$Zn + \frac{1}{2}O_2 \leftrightarrows ZnO$$

which is composed of the semi-reaction at the negative pole (-)

$$Zn + 4\,OH^- \leftrightarrows Zn(OH)_4{}^{2-} + 2e^-$$

the precipitation/solvatation reaction

$$Zn(OH)_4{}^{2-} \leftrightarrows ZnO + H_2O + 2\,OH^-$$

and the positive pole (+) semi-reaction

$$\frac{1}{2}O_2 + H_2O + 2e^- \leftrightarrows 2\,OH^-$$

where in all the reactions the lower arrow indicates the discharge process while the upper one indicates the charge process.

1.5 – Oxygen Electrode Reactions

The performance of Metal-Air batteries is strongly associated with the electrochemical reactions that occur in the cell. While the anodic one occurs in a single pathway, Oxygen Electrode reactions in alkaline media may occur in two different pathways depending on the number of electrons exchanged.

For the direct 4-electron pathway the standard reduction potential of Oxygen in alkaline media is 0.401 V vs Standard Hydrogen Electrode (SHE).

$$O_2 + 2\,H_2O + 4e^- \leftrightarrows 4\,OH^- \qquad E^0 = 0.401\,V\ vs\ SHE$$

In the 2-electron pathway, O_2 is reduced to peroxide ion,

$$O_2 + H_2O + 2e^- \leftrightarrows OH^- + HO_2{}^- \qquad E^0 = -0.076\,V\ vs\ SHE$$

followed by either further reduction,

$$HO_2{}^- + H_2O + 2e^- \leftrightarrows 3\,OH^- \qquad E^0 = 0.878\,V\ vs\ SHE$$

or disproportionation,

$$2\,HO_2{}^- \leftrightarrows O_2 + 2\,OH^-$$

In non-standard conditions, the equilibrium potential is established according to the Nernst equation:

$$E = E^0 - \frac{RT}{nF}\ln\frac{a_{Ox}}{a_{Red}}$$

where *R* is the gas constant, *T* is the temperature in Kelvin, *n* is the number of electrons transferred, *F* is the Faraday constant, and *a* is the activity of the oxidized and reduced species.

As shown in **Figure 5**, considering a Zn-air cell, once a reduction and an oxidation process are coupled, the entity of the voltage difference between the anode and cathode depends on the exchanged current. The generated potential difference during the discharge phase will be lower than the theoretical value of 1.65 V resulting in lower available power. During the discharge step instead, the imposed potential difference should overcome the standard potential value. The difference between the two values causes energy dispersion and lower efficiency.

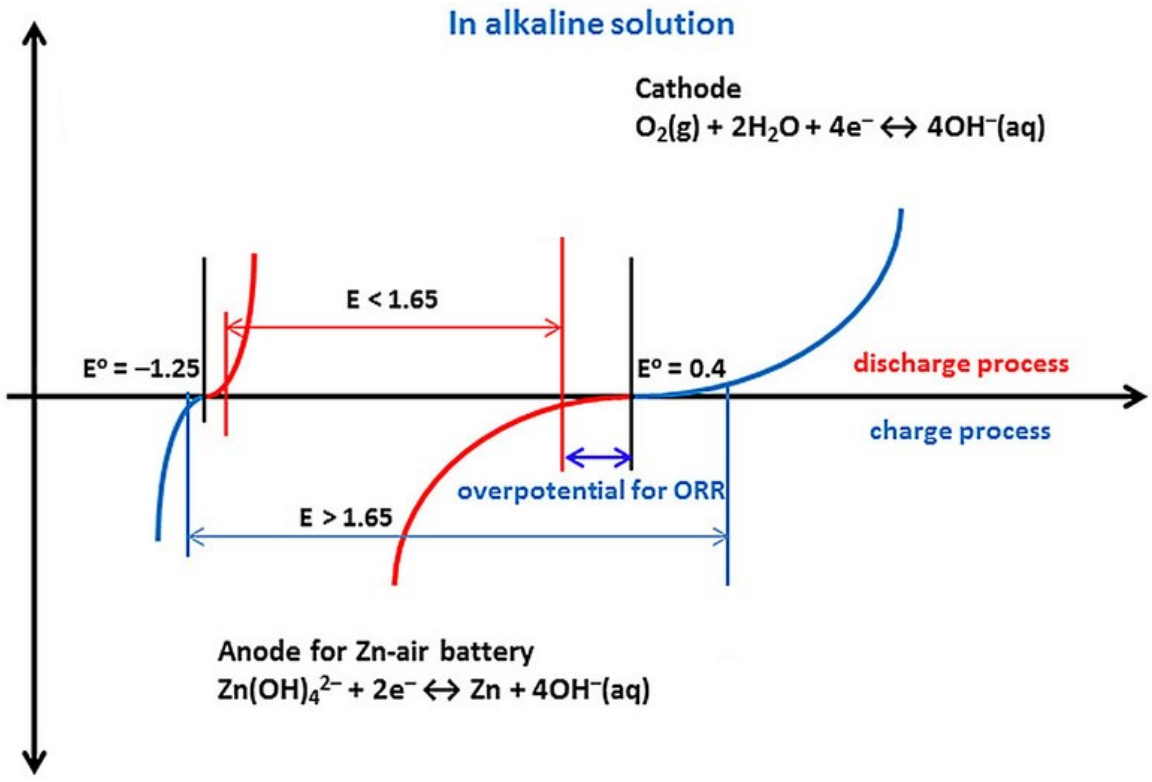

Figure 5. *Schematic polarization curves of rechargeable aqueous Zn-air batteries. The equilibrium potential is 1.65 V in an alkaline solution. Modified from ref [11]*

The deviation from ideality is directly related to the overpotential η of the two reactions, computed as the difference between the applied potential *E* and the thermodynamic potential for oxygen reduction (E^0 = 1.23 V vs SHE),

$$\eta = E - E^0$$

Generally, the entity of the overpotential is caused by several kinetic hindrances, for example, the reaction energy barrier of elementary reaction steps (activation overpotential), ohmic voltage loss (ohmic resistance overpotential), and mass transport [11]. This fact poses a severe limitation once Oxygen Electrode reactions (ORR and OER) are to be considered since they are mass-transfer dominated reactions due to oxygen's limited solubility and its low diffusion coefficient in aqueous electrolytes. Being ORR and OER kinetically sluggish, efficient electrocatalysts are highly required to accelerate this process, by decreasing the overpotentials and improving the energy efficiency. [12].

1.6 – Catalysts for Secondary Metal-Air Batteries

A variety of electrocatalyst compositions have been proposed for the air cathode ORR and OER reactions. They can be commonly classified into noble metal catalysts, transition metal oxide catalysts, phosphides and sulfides, metal phosphates and borates, carbon-based materials, and metal-organic compounds [13]. As there are two reactions with different mechanisms on charge and discharge, some catalysts are proposed for either the ORR or OER reaction, while others target bifunctional catalytic activity [14]. Such a definition can be introduced by evaluating the overpotential value shown for both reactions.

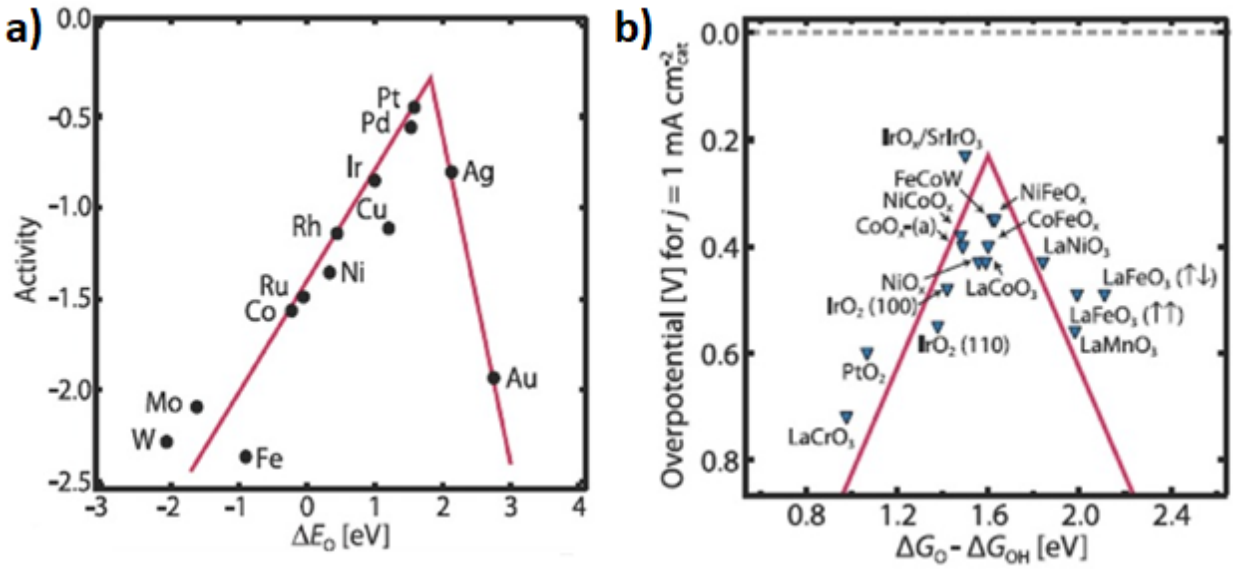

Figure 6. *Volcano plot for a) ORR and b) OER adapted from ref. [15]*

The electrochemical performances of electrocatalysts towards ORR and OER can be visually reported in a chart, named volcano plot (**Figure 6**). In a typical electrochemical volcano plot the x-axis represents a descriptor of the interaction between the catalyst and the reactant, which could be represented as standard electrode potential, adsorption energy, or some other property related to the stability of reaction intermediates. The y-axis represents the reaction rate of the specific

electrochemical reaction in terms of overpotential, current density, or some other measure of performance. Each point on the plot represents a different catalyst or catalyst composition, being the most performant the ones located at the maximum. Volcano plots for OER and ORR are reported in **Figure 6**.

Every category shows advantages and disadvantages related to the electrochemical performances, the abundance of the raw materials, their cost, the morphological and electrical properties, and the durability and stability of the catalyst. For example, though noble metals are well-known and well-studied classic catalysts, showing high catalytic activity in oxygen reactions and great stability, they are limited by their cost and scarcity, which make them unsuitable for mass-scale production. The non-metal doped carbons and carbon-transition metal hybrids are not durable because of the carbon corrosion occurring under operating conditions, caused by intermediates generated in the reaction. Transition metal oxides show insufficient ORR activity and have generally a poor electrical conductivity. Moreover, incorporating carbon additives to improve this criticality causes the same carbon corrosion problem [16].

1.7 – Single Atom Catalysts

One of the strategies recently adopted to overcome the reported issues is the use of single-atom catalysts (SACs). These kinds of heterogeneous catalysts are constituted by individual metallic atoms dispersed onto a support. The dispersion produces an increase in the metal exposed surface area, maximizing the efficiency of metal-atom use. Still, the reduction of catalytic sites was also demonstrated to increase the catalytic activity and selectivity compared to nanoclusters and nanoparticles. The support can be constituted by carbon-based materials, such as activated carbon, graphene, or carbon nanotubes (CNTs), metal oxides, or Metalorganic Frameworks (MOFs).

Unfortunately, SACs are often unstable and tend to aggregate because of the high surface energy of the atomically dispersed metal atoms, which enhances their mobility on the support surface [17]. This condition may be aggravated during the catalysis stage since new interactions and intermediates are formed due to the applied potential. To improve the stability of the catalyst, the support must be able to strongly stabilize the metal atoms avoiding their agglomeration. This could be achieved by establishing strong metal-support interactions, and/or decreasing the mobility of single atoms [18]. In general, considering transition metals, the metal active site coordination with the support is achieved using moieties containing heteroatoms such as oxygen, nitrogen, and sulfur [19]. The nature of such an environment also affects the activity of the SACs [20].

Recently the effect of the introduction of different atomic species within a single atom has been investigated. In this kind of novel atomically dispersed metal catalysts (NADMCs), active sites feature two or more catalytic centers. Dual atom catalysts (DACs) are included in such a category. They are constituted by two individual metal atoms dispersed on a support material and involve the formation of metal-metal bonds between them. The precisely designed structures of these multicomponent SACs are expected to be responsible for the synergistic optimization of the overall electrocatalytic performance by beneficially modulating the electronic structure, the nature of orbital filling, the binding energy of reaction intermediates, the reaction pathways, and the local structural transformations [21]. These contributions allow the overall increase of activity, selectivity, stability, and efficiency of the electrocatalyst once compared to conventional SACs.

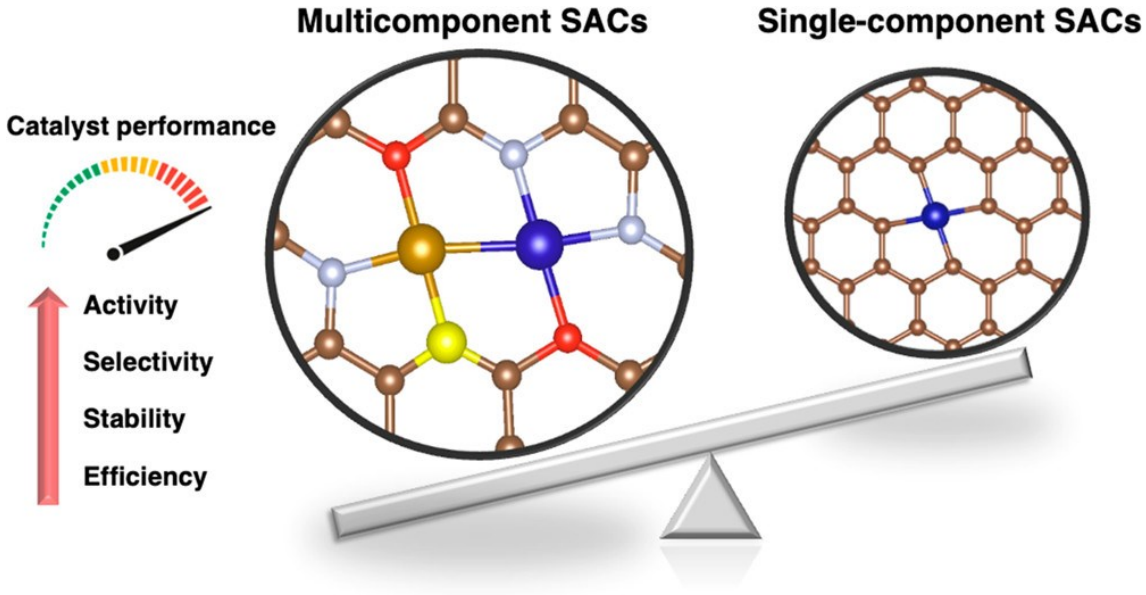

Figure 7. *Comparison between SACs and multicomponent SACs adapted from ref [19]*

Due to multiple neighboring active sites, NADMCs could also exhibit much higher activity and selectivity than SACs, especially in complicated reactions with multi-step intermediates [22]. NADMCs, and subsequently DACs, are then perfect candidates to be investigated towards the increase of ORR and OER performances of electrocatalysts.

In this thesis, the synthesis of a DAC based on Iron and Manganese and its activity towards Oxygen electrode reactions was investigated. Fe and Mn were chosen thanks to their already demonstrated activity for ORR and OER and due to their great abundance and low toxicity. The active sites were chosen to be supported onto Nitrogen-doped carbon nanotubes since this structure has an exceptional specific surface area, great chemical and physical inertia, and excellent electrical conductivity.

The aim of this work was to propose a reversible catalyst for OER and ORR in an environment similar to the one present in Zinc-Air batteries. The chosen synthesis strategy was a single-step thermal process, anticipated by the coordination of the metallic cations with the CNTs. The realized materials were then tested considering their performance and activity towards OER and ORR in an electrochemical cell. The effect of the metal ratio between Fe and Mn was also evaluated.

CHAPTER 2 – Materials Synthesis and Characterization Methods

2.1 – Material Synthesis

Multi-walled carbon nanotubes (MWCNTs) were initially subdued to a functionalization treatment to create superficial hydrophilic groups. 200 mg of MWCNTs were initially dispersed in a 52 mL solution of concentrated H_2SO_4 and HNO_3 in a 3:1 volume ratio in a volumetric flask and sonicated for 30 minutes. Subsequently, the mixture was left stirring at room temperature for 24 hours. After filtering and several washing steps in milli-Q water up to neutralization, MWCNTs were once again stirred for 24 hours in 25 mL of 5M HNO_3. Following filtration and washing in milli-Q water MWCNTs were dispersed in milli-Q water. The mixture was then frozen, and water was removed by freeze-drying. The resulting functionalized carbon nanotubes were labeled as *CNThydro* and were employed in the synthesis of all the studied materials.

To synthesize the analyzed catalysts, 20 mg of *CNThydro* were dispersed together with 63 mg of Melamine and a variable amount of metal-containing solution in 50 mL of milli-Q water and sonicated for at least 30 minutes. The mixture was then left stirring overnight (for at least 15 hours) at 50 °C, and once again sonicated for 2 hours. After this, water was removed by freeze-drying to preserve the high superficial area of the original material. The dried powder was placed in an alumina boat and underwent a high-temperature treatment in a nitrogen atmosphere. Such treatment consisted of heating up to 400 °C at 2°C/min, 30 minutes at a constant temperature of 400°C, followed by a second heating ramp of 5°C/min up to 800 °C and soaking for 2 hours at the same temperature.

The resulting powder was then etched in a solution of 1 M H_2SO_4 at 100°C under stirring to remove the eventual nanoparticles formed during the high-temperature process. Both physicochemical and electrochemical characterization were performed on samples both before and after the etching.

Five different categories of carbon nanotube-based catalysts were synthesized, depending on the quantity of Iron and Manganese in the sample. A sample without any added metal was synthesized as a control. The metal content in the sample, where present, was fixed to 1 mg, i.e. 5wt% of the carbon nanotubes content. The samples were named considering the atomic ratio Fe: Mn present in the material. A summary of the metal content and the designation of each not-etched material can be found in **Table 2**.

Table 2. Designation and nominal composition of the synthesized materials

Material	Metal content (wt%)	Fe (wt%)	Mn (wt%)
N-CNTs	-	-	-
N-CNTs-Fe	5	5	-
N-CNTs-Mn	5	-	5
N-CNTs-Fe_1Mn_1	5	2.5	2.5
N-CNTs-Fe_2Mn_1	5	3.7	1.3

Multi-walled carbon nanotubes (>98% carbon basis), Manganese (II) Chloride tetrahydrate (>98%), Iron (III) chloride hexahydrate (>98%), melamine (99%), Potassium hydroxide (90%), Nafion (5wt% solution), isopropanol (>99%), ethanol (>99.9%), sulfuric acid (95.0-98.0%) and nitric acid (99%) were purchased from Sigma-Aldrich. All chemicals were of commercial purity and were used without further purification. All water used for cleaning and preparing the electrolyte solutions was demineralized and ultrafiltered by a Millipore Milli-Q system (resistivity 18.2 MΩ).

2.2 – Physicochemical Characterization Methods

The synthesized CNTs-based catalysts were characterized using X-ray diffraction, Transmission Electron Microscopy, and X-ray photoelectron Spectroscopy. A brief description of each analysis technique is reported in the following paragraphs.

2.2.1 Transmission Electron Microscopy

Transmission Electron Microscopy (TEM) and Scanning Transmission Electron Microscopy (STEM) serve as instrumental techniques for unveiling the structures of materials at the atomic scale [23]. Both methodologies rely on the interaction of a highly energetic electron beam with atoms and their associated electron clouds. This beam is generated by an electron gun and then meticulously focused by condenser lenses and fired on the analyte, typically an electron-transparent sliver of material only tens of nanometers thick [24].

For TEM, as the electrons traverse the sample, their response is linked to the local density and composition of the material itself. Regions with higher density act as obstacles, scattering or absorbing a greater number of electrons [25]. Conversely, areas with less dense materials permit a higher proportion of electrons to pass through unimpeded. Objective lenses subsequently magnify the unaltered, transmitted electrons, reconstructing an image of the sample's internal structure.

The resulting image reveals a topographical map, where darker regions correspond to denser areas within the sample.

STEM builds upon the TEM, incorporating elements from Scanning Electron Microscopy (SEM). Similar to TEM, STEM employs an electron gun to generate a beam. However, in STEM, this beam is further concentrated into an incredibly fine probe by specialized lenses. This focused probe then can be used to analyze with high resolution the sample, scanning a well-defined region in a raster pattern. As the probe meticulously scans each point on the sample, a detector collects the high-angle scattered electrons. The intensity of these electrons at each scanned location allows the construction of a point-by-point image of the sample [26].

The contrast observed in both TEM and STEM images originates from the interaction between the electron beam and the sample. Elements with higher atomic numbers (*Z*) possess more electrons surrounding their nuclei. These dense electron shells interact more strongly with the incoming electrons, leading to a greater degree of scattering and absorption. In a TEM image, this translates to darker gray values in regions containing heavier elements. Conversely, elements with lower *Z* scatter and absorb less, allowing more electrons to pass through unhindered. These zones appear brighter with higher gray values in the image. In STEM instead, since electrons are more likely to be reflected from elements with high *Z*, heavier elements with stronger scattering will produce a stronger signal, resulting in brighter regions in the final image [27].

STEM systems can be coupled with Energy-Dispersive X-ray Spectroscopy (EDX) systems. This setup can monitor the local composition of the tested sample, creating maps of the elemental distribution within the investigated zone [28]. It relies on the emission of X-rays caused by the interaction of the high-energy electron beam generated by the STEM with the sample. The electron can knock out inner-shell electrons causing the decadence of outer-shell electrons to fill the vacancies. This is associated with the release of energy in the form of X-rays. These X-rays are characteristic of the elements that emit them and, monitoring their energy, the elemental composition of analyzed spots can be obtained.

TEM images were acquired with a JEM-F200 multi-purpose Electron Microscope. The samples were dispersed in isopropanol and deposited on a TED PELLA Lacey Carbon holder (400 mesh, Copper, approx. grid hole size: 42µm).

2.2.2 – X-ray diffraction

X-ray diffraction is a non-destructive analysis technique employed for analyzing the structure of materials, primarily at the atomic or molecular level [29]. It relies on the fact that X-rays have wavelengths in the order of nanometers, comparable with the distance between atomic planes in crystal lattices. When X-rays scatter from a substance with structure at that length scale, interference can take place, resulting in a pattern of higher and lower intensities. This pattern provides information about the internal structure on length scales from 0.1 to 100 nm.

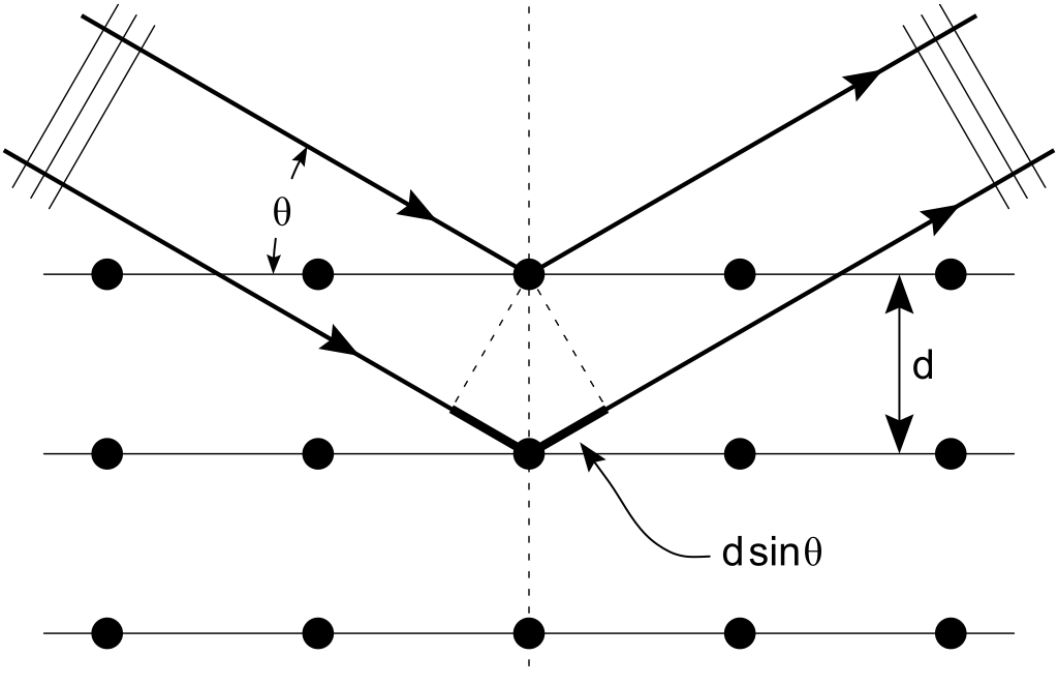

Figure 8. *Working principle of XRD*

The working principle of such a phenomenon is shown in **Figure 8**. A monochromatic X-ray with wavelength λ incident on a crystal with an angle θ can be reflected by interacting with different atomic planes, at a distance d one from another. The depth of such interaction determines a difference in the optical length traveled by the wave, which produces a difference in the phase of the wave with respect to the original one. If the path difference is equal to an integer multiple of the wavelength, then the scattered radiation will undergo constructive interference and thus the crystal will appear to have reflected the X-radiation.

This behavior is described by Bragg's Law [30]

$$n\lambda = 2d\ sin\theta$$

This correlation between diffraction angle and atomic planes distance allows us to gain insights into the measure of the distance d performing a scanning changing the incidence angle while keeping constant the wavelength λ. Such scanning results in a so-called *diffractogram* that shows the

intensity of the collected constructive interference signal as a function of twice the incidence angle 2θ, which represents the angle between the incident beam and the diffracted beam.

Since every crystalline phase shows a diffraction pattern composed of peaks located at specific 2θ angles [31], the deconvolution of a diffractogram allows to understand the phases present inside the tested sample. Moreover, considering Bragg's law, the 2θ location of the peaks provides information about the crystal lattice spacing, and so on the crystal structure. The geometric parameters of the diffraction peaks, such as peak intensity, peak location (with respect to standard), and peak broadening, can give insights into the quantitative presence of the phase in the sample, on the average crystallite size, texture, and lattice strain.

The X-rays employed for XRD analysis can be generated using different sources, such as X-ray tubes, synchrotron radiation, or radioisotope Sources. X-ray tubes are one of the most common sources used in XRD. They work based on the principle of accelerating electrons towards a target material. When the high-energy electrons collide with the target, a spectrum is generated. The spectrum is composed of *bremsstrahlung* radiation and characteristic X-ray emissions. Bremsstrahlung is caused by the deceleration or deflection of electrons caused by the positively charged atomic nuclei in the target material and is composed of X-rays with a continuous spectrum of energies. When instead incoming electrons dislodge inner shell electrons from the target atoms, causing outer shell electrons to fill the resulting vacancies, characteristic X-rays are emitted. The energy of such rays is discrete and corresponds to the energy difference between the involved electron shells. Since the emission spectrum is composed of several different radiations, filters, monochromators, and collimators are often employed to make the X-rays monochromatic and to narrow the beam of X-rays, improving resolution and reducing background noise. The wavelength employed in the XRD analysis depends on the material source and the selected emission peak. The most widely used materials are Copper, Molybdenum, Chromium, and Cobalt and generally the K_α peak is chosen since it is the most probable and brightest [32].

XRD can be applied either to pure crystals or to powders following different configurations. In the case of powders analysis, the most employed configuration is the Bragg-Brentano (θ:2θ) geometry, represented in **Figure 9**. In this setup, the source of the X-ray beam and the detector are scanned synchronously such that the incidence angle θ and the diffracted angle 2θ remain the same throughout the scanning.

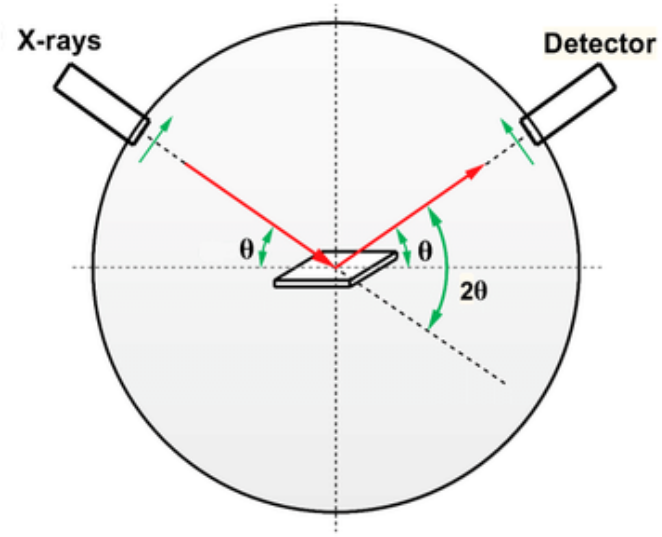

Figure 9. *Bragg-Brentano (θ:2θ) geometry adapted from ref. [33]*

Powder X-ray diffraction patterns of samples were recorded in Bragg Brentano (θ:2θ) geometry using a Bruker D8 Advance, operating with Cu Kα radiation (λ = 0.15406 nm) generated at 40 kV and 40 mA.

2.2.3 – X-ray Photoelectron Spectroscopy

X-ray Photoelectron Spectroscopy (XPS) is a technique that allows the identification of the elements that compose a surface and most importantly their chemical states. It takes advantage of the photoelectric effect described by Einstein in 1905, according to which the atoms of a sample irradiated with high enough energy photons can ionize and emit photoelectrons proportionally to the intensity of the incident light. If the photoelectron is emitted from the surface of the sample and does not undergo inelastic scattering, its kinetic energy (KE) is given by the difference between the energy of the incoming photons (hν), the energy which bound the electron to the atom, the binding energy (BE), and the sample's work function in vacuum Φ_s

$$\mathrm{KE} = \mathrm{h}\nu - \mathrm{BE} - \Phi_s$$

To detect the photoelectrons an analyzer, that measures the kinetic energy of the electron, is required. The analyzer itself possesses a work function Φ_A, which causes a shift in the measured

value of kinetic energy KE' from its real value. Since the X-ray photon energy is known, the photoelectron kinetic energy is measured, and the work function of the analyzer is empirically found, the binding energy of the photoemitted electron can be determined as

$$\mathrm{BE} = \mathrm{h}\nu - \mathrm{KE}' - \Phi_A$$

Comparing the peaks at specific binding energies that arise from a spectrum with those in literature [34], it is possible to identify which elements are qualitatively and quantitatively present in a sample. Oxidation states can be determined as well. An oxidized element has a lower electron density than its neutral or reduced counterparts, so the remaining electrons experience a lower screening of the nuclear positive charges and, thus, have a higher binding energy. The opposite goes for an element in a reduced state, in which electrons show lower binding energies due to a more effective screening given by the higher electron density. Hence, by deconvoluting a photoemission peak in its components it is possible to deduce the chemical states of a given species.

The photoemission peak shapes can vary greatly depending on the atomic orbital considered. Electrons from *s* orbitals show only one line, while electrons from *p*, *d*, and *f* orbitals all exhibit two coupled peaks due to spin-orbit coupling. The coupling between orbital and spin momentum is described by the quantum number $j = |l \pm s|$, where l defines the orbital and s the spin. The splitting typically grows with the atomic number and the degeneracy is equal to $2j + 1$. For example, a *p* orbital ($l = 1$) will present two peaks $p_{1/2}$ and $p_{3/2}$ with a constant area ratio (1:2).

The shape of a singular well-defined photoemission peak is theoretically a Lorentzian function, with a natural line width that depends on the lifetime of the core hole state left by the photoemission process. However, due to temperature-dependent atomic vibrations, complex final states, chemical environment, and instrumental broadening of the peaks, photoemission lines are better described by a convolution of a Gaussian and a Lorentzian curve.

XPS is a technique with significant surface sensitivity. Even though X-rays penetrate around one micrometer of material and so excite photoelectrons until that depth, only the ones ejected from the outermost 10 nm can emerge from the sample with a non-zero KE and reach the analyzer. Hence XPS is defined as a superficial analysis technique.

X-ray photoelectron spectroscopy (XPS) measurements were acquired in a custom-made UHV system working at a base pressure of 10^{-10} mbar, equipped with an Omicron EA125 electron analyzer and an X-ray source with a dual Al-Mg anode. Photoemission spectra were collected at

room temperature with a non-monochromatized Al Kα X-ray source (1486.3 eV). Single spectra were acquired using 0.1 eV steps, 0.5 s collection time, and 20 eV pass energy.

2.3 – Electrochemical characterization methods

Considering a generic electrochemical reaction, the dependence of the current density j on the applied potential E may be described by the Butler-Volmer equation

$$j = j_0 \left[exp\left(\frac{(1-\alpha)nF\eta}{RT}\right) + exp\left(-\frac{\alpha nF\eta}{RT}\right)\right]$$

where j_0 is the exchange current density, α is the charge transfer coefficient, n is the number of electrons involved in the reaction, F is the Faraday constant, R is the universal gas constant, $T$is the absolute temperature, and η is the overpotential given by the difference of the applied potential and the equilibrium one E_{eq}. The exchange current density is the current density passing through an electrode in both directions when the overpotential and the net current density are null and can be described with the equation

$$j_0 = nFC_0^* K^0 \exp\left(-\frac{\alpha nF\left(E_{eq} - E^O\right)}{RT}\right)$$

where C_0^* is the concentration of the consumed reacting species, K^0 is the standard kinetic constant of electron transfer and E^O is the standard electrode potential.

In the case of a reaction not limited by mass transfer, for large overpotential, either cathodic or anodic, there is a linear proportionality between the logarithm of the current density and the overpotential applied. The Tafel equation describes this dependency.

$$\eta = a + b\log|j|$$

Describing the overpotential as a function of the logarithm of the current with a linear equation, the slope b of this equation is commonly described as the Tafel slope. The determination of the Tafel slope is crucial in the description of a reaction's kinetics since this parameter gives an account of the mechanism of an electrochemical reaction. The value of the Tafel slope may also be exploited to refer the electrochemical reaction to intermediate reactions or steps. The value of the Tafel slope, in fact, is related to the less favored step occurring in the reaction and the comparison with theoretical studies and well-known intermediate reactions may identify the Rate Determining Step of the reaction [35].

Going outside Butler-Volmer theory, the entity of the evolved current also depends on the concentration of the species participating in the reaction in the proximity of the electrode. Reactions where the rate of the reaction is primarily determined by the transport of reactants or products to or from the electrode surface are named mass transfer-controlled reactions. In these reactions, assuming that the kinetics of the charge transfer are rapid, the concentration of the reduced and oxidized species can be assumed to be in equilibrium with the applied potential. Considering a generic mass transfer-controlled reaction, the current density can be described through the Koutecky-Levich equation as

$$\frac{1}{j} = \frac{1}{j_K} + \frac{1}{j_L}$$

where j is the measured current density, j_K is the kinetic current density, modeled by the Butler Volmer equation, and j_L is the mass transport current density, which can be described according to the electrochemical setup used. One of the most widespread setups used to describe this contribution is the rotating disk electrode (RDE) setup. In this configuration the electrode rotates during the experiment, inducing a flux of analyte to the surface of the electrode. The mass transport current density can be modeled as [36]

$$j_L = B\ \omega^{0.5}$$

where ω is the angular rotation rate of the electrode and B is the Levich constant, defined as

$$B = 0.62\ n\ F D^{2/3} \nu^{-1/6} C$$

with n being the number of electrons involved in the reaction, F is the Faraday constant, D is the diffusion coefficient [$cm^2 s^{-1}$], ν is the kinematic viscosity [$cm^2 s^{-1}$] and C is the analyte concentration [$mol\ cm^{-3}$].

ORR is a mass transfer-controlled reaction and, as previously seen, this reaction may occur in the 2-electron or in the 4-electron mechanism in an alkaline environment. To monitor the number of electrons exchanged, and thus the goodness of the catalysts tested, the Koutecky-Levich analysis can be performed. In this analysis, linear sweep voltammetries (LSVs) are performed using an RDE at different rotation rates. At a fixed potential, the inverse of the measured current densities at each different rotational speed may be plotted against the inverse of the square root of the angular rotation rate. Performing a linear fitting for the resulting distribution, the slope resulting from the

fitting can be employed to calculate the number of exchanged electrons recalling the definition of B.

Another widespread technique to evaluate the preferential mechanism of the ORR is the rotating ring-disk electrode (RRDE). In this setup two working electrodes, separated by a non-conductive barrier, are present. In the case of ORR, at the disk, the ORR reaction is performed by measuring the current while varying the applied potential. The ring instead operates at a fixed potential at which the hydrogen peroxide, developed at the disk and supplied to the ring by the centrifugal motion, can be oxidized back into water. There are equations that correlate the values of the ring current I_r and disk current I_d to the hydrogen peroxide yield $H_2O_2(\%)$

$$H_2O_2(\%) = 200 \times \frac{I_r}{I_d + N\, I_r}$$

and to the number of exchanged electrons n

$$n = 4 \times \frac{I_r\, N}{I_d + N\, I_r}$$

where N is named current collection efficiency and depends on the geometrical rations between disk, ring, and their distance in the employed electrode tip.

The first step of the electrochemical characterization was the preparation of an electrochemical ink for each material. The ink was prepared by dispersing 1mg of the tested catalyst into 200 µL of Milli-Q water, 50 µL of ethanol, and 3 µL of Nafion-containing solution and sonicating for at least 30 minutes. The produced ink was then deposited on the glassy carbon of a Metrohm RDE (diameter 3mm) and RRDE (diameter 5mm) to obtain a homogeneous film. The loading of the catalyst was chosen to be 0.56 mg cm^{-2} in both cases.

Electrochemical measurements were carried out in a three-electrode electrochemical cell in KOH 0.1M solution in a polypropylene cell. A glassy carbon coated with the catalyst ink served as the working electrode, while a Pine Research Hg/HgO electrode and a graphite rod were used as reference and counter electrode, respectively. The signal was acquired using an Autolab PGSTAT204 potentiostat by Metrohm. The rotation rate of the working electrode was imposed using a Metrohm Autolab Motor controller unit.

OER was performed using an RDE tip, saturating the electrolyte in oxygen and recording subsequent cyclic voltammetries (CVs) at a fixed rotating speed of 1600 rpm. The CVs acquired a single scan

from 0.1 V vs ref. to 1.0 V vs ref with a 5mV sec^{-1} step and were repeated until the i-V curves were stable.

ORR was performed using an RRDE tip. The electrolyte solution was first saturated in nitrogen. A stabilization of the material was then performed acquiring 50 CVs in the range -0.86 - -0.17 V vs ref at 200 mV sec^{-1} at 1600 rpm. Three CVs were then performed in the range -0.86 - 0.23 V vs ref at 5 mV sec^{-1} in a static configuration. The same CVs measurement was then repeated after the electrolyte solution was saturated in oxygen. The ORR was investigated performing LSVs at 200, 400, 600, 900, 1200, 1600, 2000, 2200, and 2500 rpm from 0.3 V vs ref to -0.9 V vs ref at 5 mV sec^{-1}. These measurements were performed in no particular order. Oxygen was bubbled in the solution for 60 seconds between two consecutive LSVs to ensure the saturation of the electrolyte. During the LSVs, the potential at the Pt ring was fixed at 0.55 V vs ref.

In all measurements, the potential was corrected to account for the ohmic drops in the electrolyte. The value of the corrected potential $E_{Hg/HgO}$ was then converted in V vs RHE E_{RHE} with the following formula

$$E_{RHE} = E_{Hg/HgO} + 0.0592\,pH + E^{O}_{Hg/HgO}$$

were $E^{O}_{Hg/HgO}$ is the standard electrode potential for Hg/HgO (0.098 V) and the pH value was assumed to be 13.

The Koutecky-Levich analysis was performed using a self-produced Python script. The calculation of the Levich constant was done considering the involved parameters as constants with the values respectively of concentration of O_2 (1.2×10^{-6} mol cm^{-3}); diffusion coefficient of O_2 (1.9×10^{-5} cm^2 s^{-1}); kinematic viscosity of the electrolyte (0.01 cm^2 s^{-1}).

CHAPTER 3 – Experimental results

In this chapter, the results obtained from both the physicochemical and electrochemical characterization of the synthesized materials are presented and discussed.

3.1 – Physicochemical characterization

The morphology of the synthesized materials was first investigated by (scanning) transmission electron microscopy (STEM and TEM). The functionalized CNTs, *CNThydro,* were analyzed and the results are reported in **Figure 10**. The TEM image evidences the presence of nanoparticles of a few nanometers, preferentially located towards the end of the nanotubes but also situated inside the cavity (**Figure 10a**). To evaluate the elemental composition of the nanoparticle, EDX analysis is performed (**Figure 10b**) highlighting the prevailing presence of Cobalt. The nanoparticles are then considered to be a residual of the catalysts employed for the synthesis of MWCNTs that were not removed due to being enclosed within the nanotubes. Analyzing the trend in the pixel's gray value and performing the Fast Fourier Transform (FFT) of the nanotube wall (region A) and the nanoparticle (region B), it is possible to determine the spacing between the crystalline plains. The distance between the graphitic layers was 0.34 nm, in agreement with the results reported in the literature [37]. The distance of the lattice fringes in region B is around 0.21 nm, which corresponds to the cobalt (111) interplane distance [38].

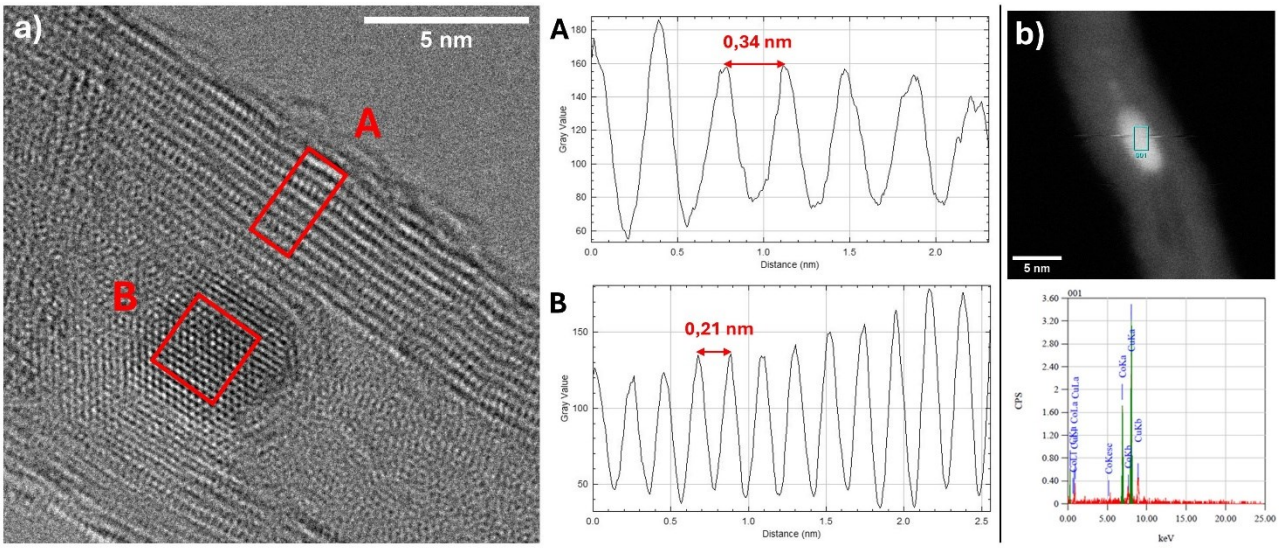

Figure 80. *a) TEM image of Cobalt based nanoparticle and of CNTs wall. The gray values distribution of region A (CNT) and B (NP) are also reported. b) STEM imaging of the identified nanoparticle and respective EDX spectrum*

The analysis of N-doped CNTs enforced the stability, that was unaltered after the thermal treatment, and the presence of the Co catalysts. The introduction of nitrogen cannot be monitored through

contrast since carbon and nitrogen atomic numbers differ only by 1 nor by EDX since their characteristic emissions are similar.

The typical morphology of the metal-modified sample before the etching treatment is reported in **Figure 11**. In this case, there is a clear presence of nanoparticles, represented by bright spots in **Figure 11a** and by dark zones in **Figures 11b** and **11c**, that seem to decorate the CNTs. These nanoparticles show a wide variety in their size distribution, ranging from nearly 25 nm down to less than 10 nm. Considering the N-CNTs-Fe_2Mn_1 sample, the evaluation of the distance between the atomic planes of the nanoparticles returns an average value of 0.25 nm, which agrees with the literature values for $MnFe_2O_4$ (311) planes [39].

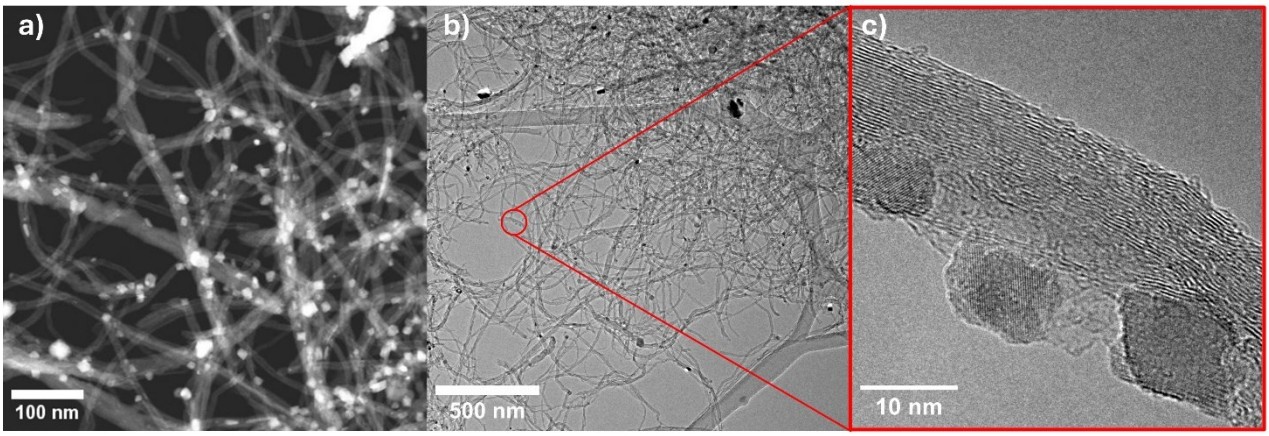

***Figure 11**. Images of N-CNTs-Fe_2Mn_1 before etching. a) STEM image b) TEM image c) High magnification TEM image*

During the analysis, a larger number of nanoparticles confined by the CNTs were identified. To evaluate the nature of these nanoparticles and to determine the elemental composition of the nanoparticles at the surface of the CNTs, an EDX map was acquired (**Figure 12**).

The EDX mapping allowed us to identify the presence of both Fe and Mn in the nanoparticles (NPs) at the surface and in the cavities of the CNTs. The mapping also allowed us to monitor the presence of oxygen in the nanoparticles, highlighting that the non-confined ones show a higher oxygen content and are presumably constituted by oxides. The NPs located in the cavity instead show a lower oxygen content and should then be characterized by a reduced state, either metallic or less oxidized state. Fe and Mn are simultaneously present in some of the investigated nanoparticles, suggesting the presence of mixed oxides and alloys. Some inner nanoparticles show the preferential presence of one of the metallic species. Overall, no specific phase is identified, since both mixed and pure oxides and metal were detected. The EDX also evidences the presence of sulfur. This contamination may be caused by the sulfuric acid employed in the functionalization of the CNTs with hydrophilic groups. Sulfur is preferentially bonded with metals in the nanoparticles. Its

presence is more relevant in nanoparticles that show a high manganese content. The formation of this manganese sulfide may be caused by the exposure of the material to high temperatures during the thermal treatment.

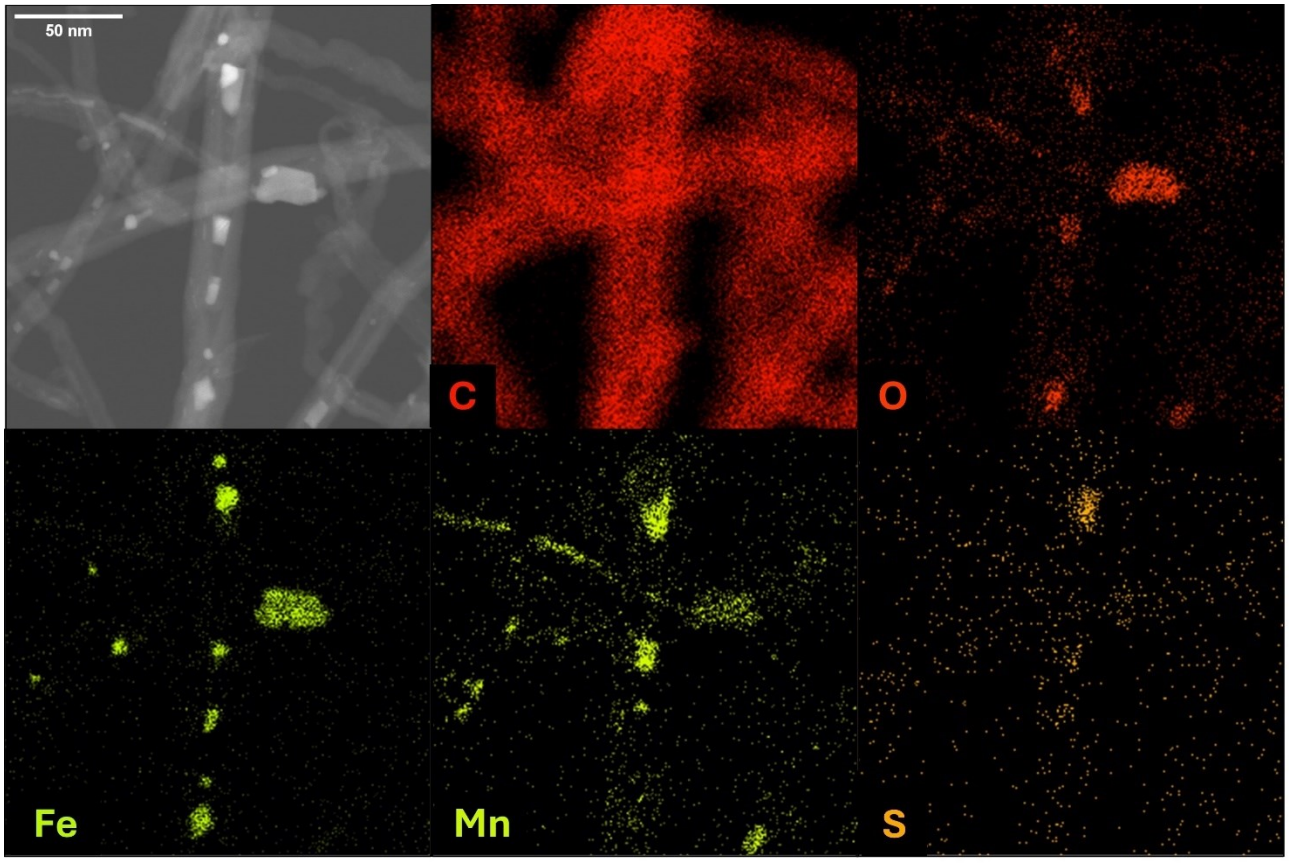

Figure 12. *EDX map of N-CNTs-Fe_2Mn_1 before etching*

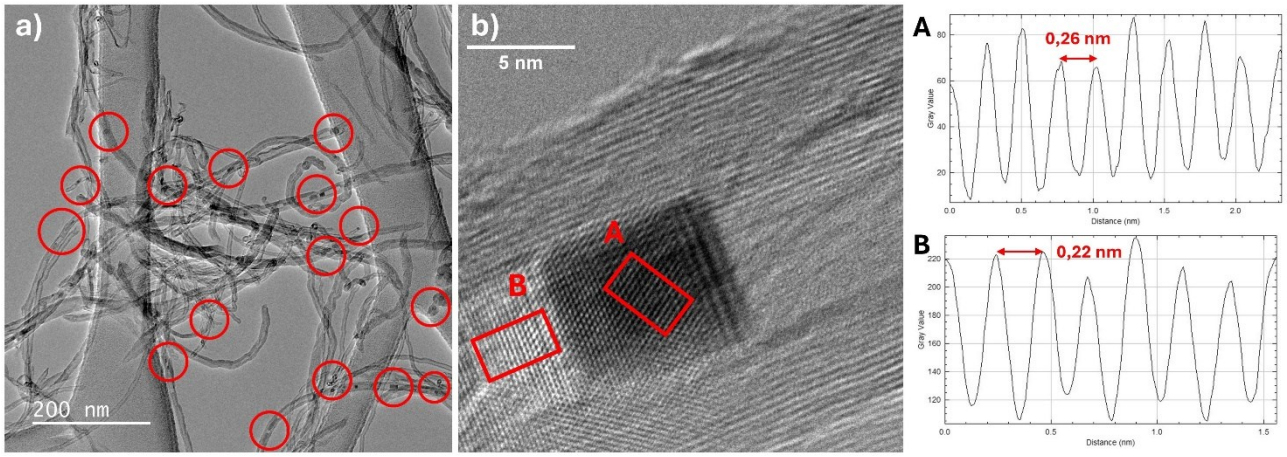

Figure 13*. TEM images of post-etched N-CNTs-Fe_2Mn_1 a) Morphology of the material, with confined NPs encircled in red b) High magnification TEM image of a confined NP. The gray values distributions of region A and B are reported.*

TEM images were also acquired on samples after the etching treatment. These samples no longer present nanoparticles decorating the CNT surface, confirming the success of the acid treatment (**Figure 13a**). However, nanoparticles confined within the nanotubes are still detected by the TEM

images (**Figure 13b**). This result confirms the resilience of these inner nanoparticles to the acid treatment and should be related to the barrier provided by the CNTs.

The composition of the resilient nanoparticles is investigated by performing an EDX map, shown in **Figure 14**. The EDX confirms the contemporary presence of metallic and oxide nanoparticles. NPs with only one or two metals are found. No sulfur is detected in samples after the etching phase, pointing out that the contamination is effectively removed with the acid treatment.

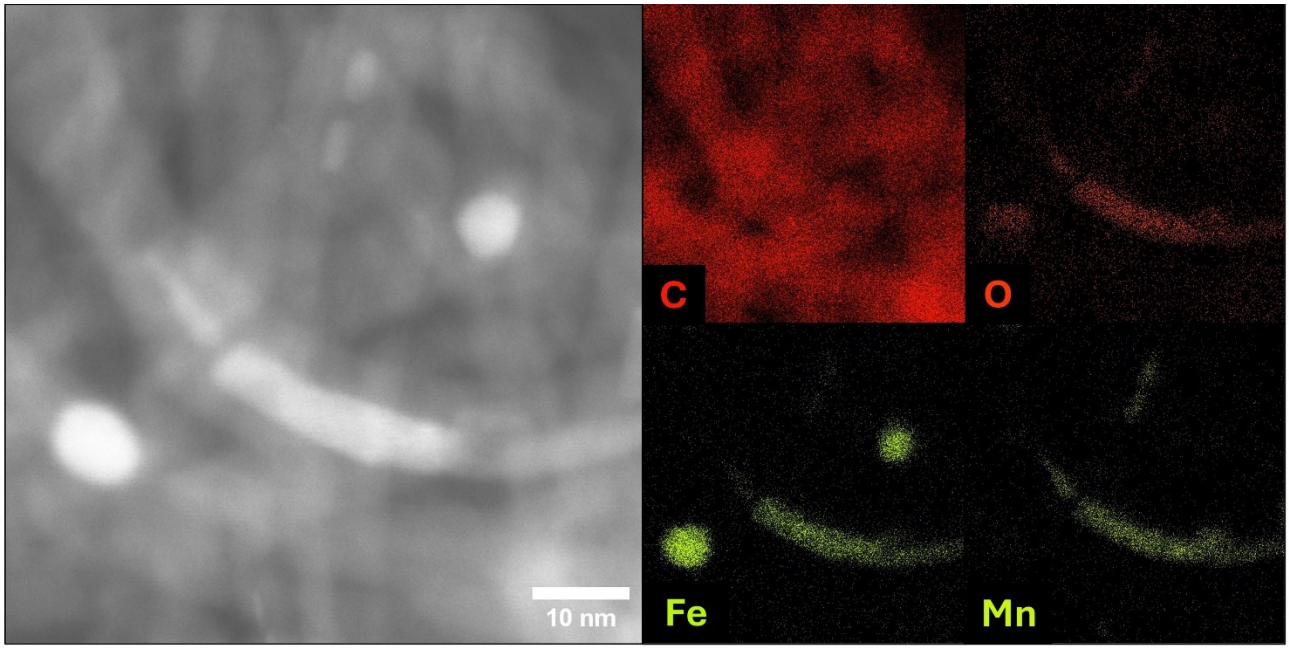

Figure 14. *EDX map of N-CNTs-Fe_2Mn_1 after etching*

The distance between the atomic planes of the non-confined nanoparticles is investigated as previously done, determining the variation of the gray values of the pixels in the image, and performing an FFT of the zone of interest (**Figure 13b**). The spacing resulted in 0.26 nm, in agreement with the value found for non-confined nanoparticles in the same sample before the etching, and of 0.22 nm, which can be associated with the (400) crystalline orientation for the same phase [40].

Since the employed TEM was not equipped with the aberration correction, during the TEM analysis it was not possible to evaluate the presence of single atoms. This impossibility characterized also to the EDX mapping since the measurement shows considerably high noise for the investigated metallic species since Fe and Mn, as well as Cr and Co, are present in the metallic alloy the TEM chamber is made of.

The samples were analyzed by X-ray diffraction (XRD) to determine the nature of the different crystalline phases present in the material. The XRD diffractograms of the materials before the etching treatment are reported in **Figure 15**.

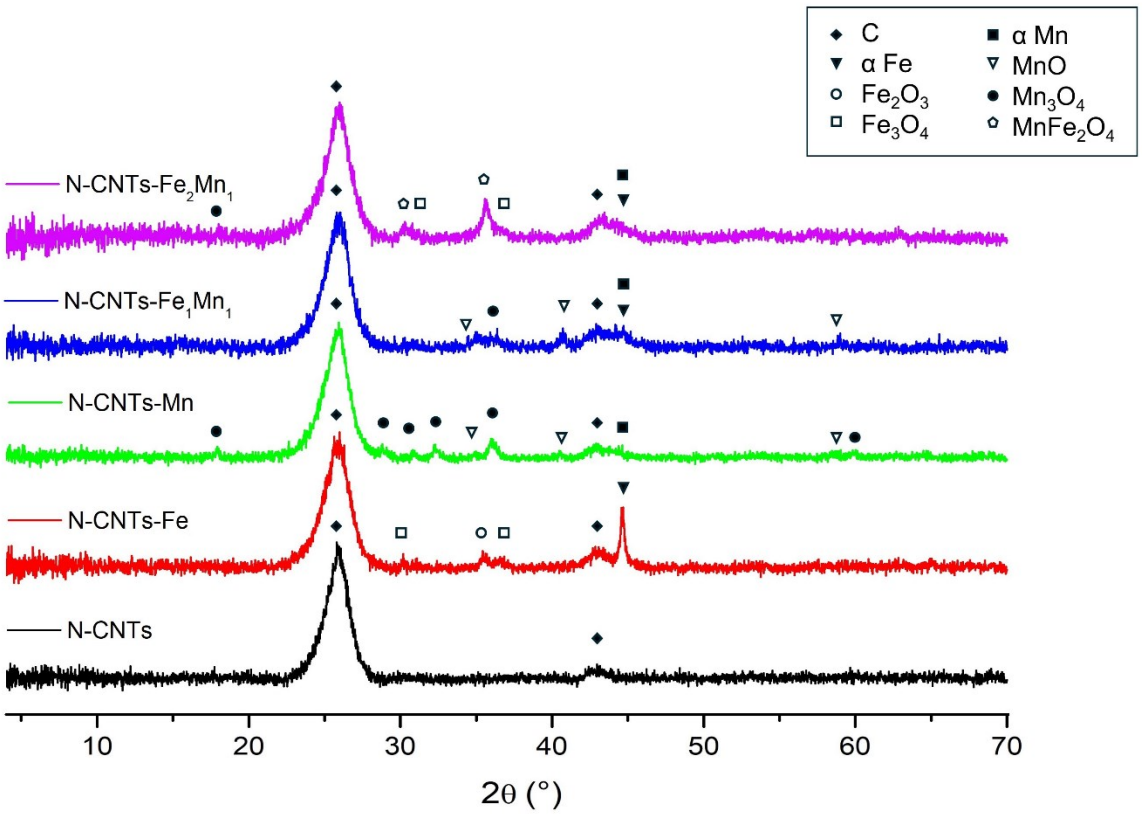

Figure 15. *XRD diffractograms for materials before etching*

The XRD patterns show two consistent peaks at 2θ values of 26° and 42°, which are assigned to the (002) and (101) peaks of carbon and are related to the spacing between the atomic planes of CNTs [41]. Metal-modified CNT samples present additional peaks related to the metallic phases. The nature and intensity of each peak depend on the metallic elements within the sample and their atomic ratio. N-CNTs-Fe presents a sharp peak at 44.6° associated with alpha iron, a few lesser peaks at 35.4° related to Fe_2O_3, and 30° and 36.5°, corresponding to Fe_3O_4 [42, 43, 44]. In N-CNTs-Mn several different secondary peaks are present. The identified crystalline phases are alpha manganese (44.6°), MnO (34.7°, 40.6°, 58.6°) and Mn_3O_4 (28.7°, 30.4°, 32.3°, 36°, 60°) [45]. The N-CNTs-Fe_1Mn_1 were affected by higher noise if compared to the others so only the main phases could be identified. The nanoparticles in this sample were identified as composed of MnO, Mn_3O_4, and of alpha iron/manganese. It was not possible to identify the presence of single metal species and their alloys since they show a very similar crystalline structure and, thus, a practically identical diffraction spectrum. Finally, considering N-CNTs-Fe_2Mn_1 the ratio Fe/Mn (2:1) allowed the preferential

formation of a mixed spinel $MnFe_2O_4$ whose peaks are located at 30.3° and 35.7° [46]. These peaks show some kind of asymmetry, with the higher-angle slope presenting some kind of *hump*. This effect was assumed to be caused by the presence of Fe_3O_4 whose peak positions are compatible with the position of the *hump*. Since iron and manganese were added with a 2:1 atomic ratio, assuming that the cations interact in the same way with CNTs in the impregnation step, the presence of a stoichiometric compound and a Fe-only phase allows us to hypothesize the presence of Mn-only phases, though no peaks associated with these phases were diagnosed in the survey. The presence of Mn_3O_4 itself is not excluded since the dominant peak at 36° could be hidden by the mixed spinel one and lesser peaks could be confused with the noise of the measurement.

Materials after the etching treatment only show the presence of the characteristic diffraction peaks of CNTs at 26° and 42° (**Figure 16**), confirming the removal of the metallic NPs as seen by TEM. These samples contain a small amount of metal-based NPs inside the CNTs. Therefore, the absence of the diffraction peaks related to these nanoparticles can be justified considering the very low amount of these phases.

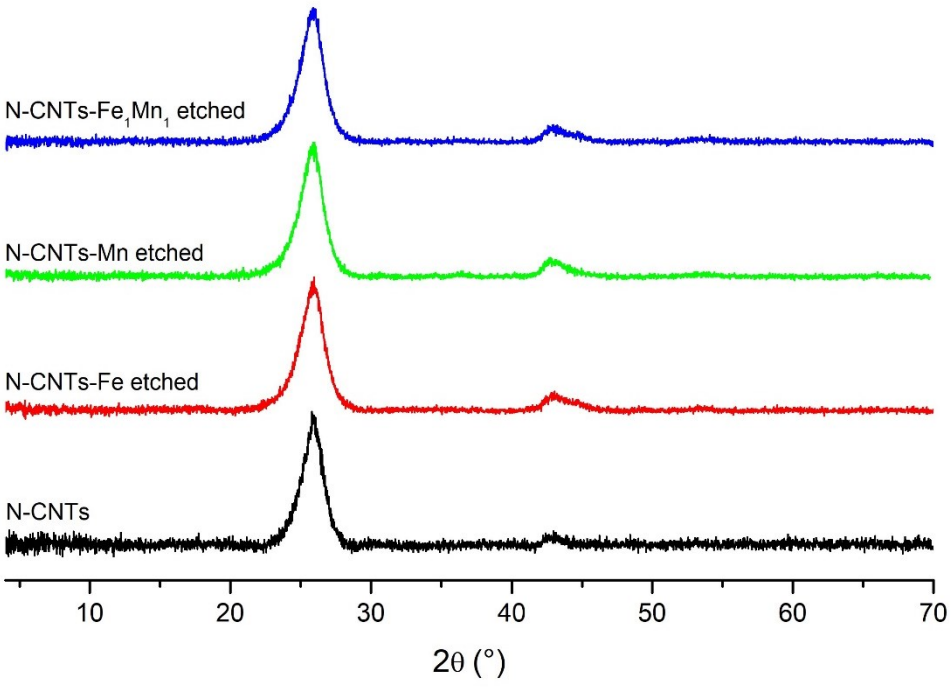

Figure 16. *XRD diffractograms for metal-modified materials after the etching. The pattern for N-CNTs is referred to the sample before the etching.*

Considering Bragg's Law there is a mathematical correlation between the distance between the atomic planes and the diffraction angle. In the hypothesis of first-order diffraction (n=1), we can say that

$$\lambda = 2d\ sin\theta$$

Inverting the relation, it is possible to determine the distance between the atomic planes given the diffraction angle and the wavelength of the utilized X-ray beam. By doing so, utilizing the diffraction angle of the identified phases distances comparable with those obtained in the TEM samples. The values calculated from the diffraction peak positions are presented together with the ones determined in the TEM analysis in **Table 3**.

Table 3. Crystalline plane distances (*d*) in **nm** calculated from XRD data through Bragg's Law, determined from the TEM analysis and literature.

Crystalline phase	**Peak position**	**Bragg's Law *d***	**TEM *d***	**Literature *d***
CNTs	25.9	0.344	0.34	0.35
Cobalt	44.2 [38]	0.205	0.21	0.203
$MnFe_2O_4$ (311)	35.6	0.252	0.25, 0.26	0.25
$MnFe_2O_4$ (400)	43.1	0.210	0.22	0.21

This procedure applied to nanoparticles confined in the CNTs allows us to confirm that the phase present in the nanotubes ($MnFe_2O_4$) is the same as the one identified in the XRD analysis.

Samples were also analyzed by X-ray photoemission spectroscopy (XPS) to determine the chemical species at the surface and the oxidation states. In particular, the C 1s, N 1s, O 1s, Mn 2p, and Fe 2p regions were acquired.

The C 1s spectrum was deconvoluted into five chemically shifted components related to C-C sp^2 and sp^3 bonds, alcohol groups (C-OH), carbonyl groups (C=O), and carboxylic groups (C=OOH). The pi*-pi transition was also included in the fit since CNTs are a graphitic carbon material. The results of the fitting stage of the different materials are then compared considering the BE and the relative presence of the species.

Figure 17 compares the C 1s region for the two non-metalated samples, *CNTs hydro* and N-doped CNTs. Both of them show the most intense peak at 284.3 eV, associated with sp^2 hybridized carbon atoms, and the peak related to sp^3 carbon atoms at around 284.8 eV. These two species are also present in the same proportion in the two samples around 76.8 - 78.5 at.% and 7.7 - 7.8 at.%, respectively. The C sp^2 component in the N-CNTs was expected to shift towards higher BE due to the interaction with N, which is more electronegative than C (3.04 of N versus 2.55 of C). This effect is not observed in the XPS data due to the low nitrogen content in the material [47]. The increase in the BE of the sp^3 C for the N-CNTs could be related to the introduction of nitrogen in the material. In fact, N–C (associated with graphitic, pyridinic, and/or pyrrolic nitrogen) is reported to show a BE in the range 285.2 - 285.7 eV [48]. The presence of this chemical species can motivate the shift of the sp^2 C towards higher BE. However, the presence of nitrogen is difficult to determine from the C 1s peak since the C-N component overlaps with the C-OH one [49]. Since the BE of the C-OH bond is the most similar to the range of the N–C bond, this peak will be further identified as C-OH/C-N in nitrogen-containing materials.

The percentage of alcohol, carbonyl, and carboxylic groups, located respectively at 286.2 eV, 287.7 eV, and 289.0 eV slightly decreases in the N-CNTs sample probably due to the decomposition of the oxygenated species during the thermal treatment, and it is confirmed from the elemental quantification performed from the XPS results. The atomic fraction of oxygen goes from 4.2 at.% to 3.7 at.%. This decrease is associated with a reduction in the presence of oxygen-containing groups (alcohol, carbonyl, and carboxylic) that undergo a proportional reduction.

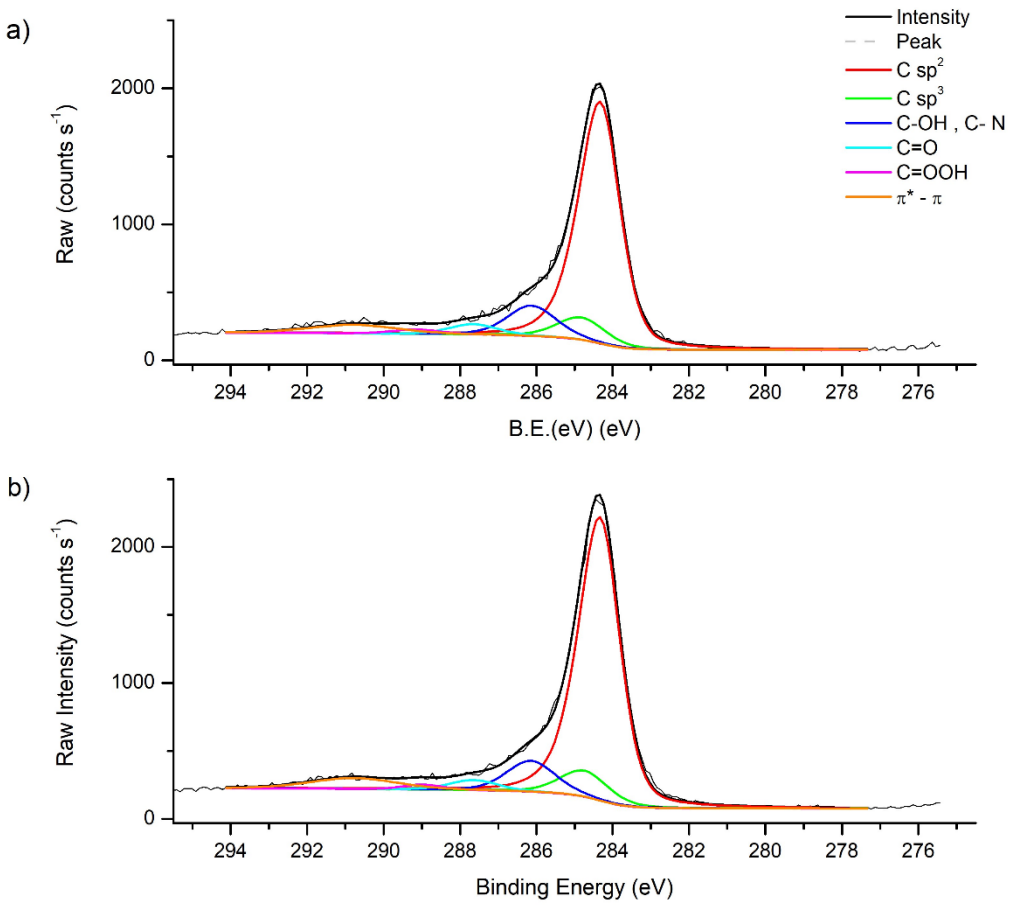

Figure 17. *C1s XPS region, and its deconvolution into chemically shifted components, for a) CNTs hydro and b) N-CNTs*

A further comparison is carried out between samples containing metals before and after the acid etching (**Figure 18**). The BE and the percentage presence of each chemical species are also reported in **Table 4**, together with the peak parameters for CNTs hydro and N-CNTs.

The same five components were used for the analysis of the C 1s region of the metalated samples. No changes in the BE were observed after the addition of the metals. Components related to C sp2, C sp3, C-OH/C-N, and C=O were observed at 284.3 eV, 284.8 eV, 286.2 eV, and 287.6 eV, respectively. The C=OOH component shows a wider variation of BE in the range 288.8 - 289.2 eV. Considering the effect of the acid treatment, we can notice that etched samples show a higher presence of (C-OH, C-N), C=O, and C=OOH. This effect could be caused by the oxidizing effect of sulfuric acid and favored by the high temperature during the etching process. Regarding the stoichiometry, a slight increase in the C sp3 component is observed after the addition of the metals.

Table 4. *BE (in eV) and atomic percentage (%) of carbon chemical species from the analysis of the C 1s XPS region*

Material	**C sp^2**		**C sp^3**		**C-OH, C-N**		**C=O**		**C=OOH**	
	B.E.	*%*	*B.E.*	*%*	*B.E.*	*%*	*B.E.*	*%*	*B.E.*	*%*
CNThydro	284.3	76.8	284.9	7.7	286.2	10.5	287.7	3.5	289.2	1.5
N-CNTs	284.3	78.5	284.8	7.8	286.2	9.3	287.6	3.1	289.0	1.3
N-CNTs-Fe	284.3	77.2	284.9	8.5	286.2	9.9	287.7	3.6	289.2	0.8
N-CNTs-Fe etched	284.3	77.5	284.9	8.4	286.2	9.3	287.7	3.4	289.2	1.5
N-CNTs-Mn	284.3	78.5	284.9	7.9	286.2	9.4	287.7	3.3	288.9	1.0
N-CNTs-Mn etched	284.3	76.7	284.9	7.5	286.2	10.0	287.7	3.7	289.2	2.1
N-CNTs-Fe_1Mn_1	284.3	77.0	284.9	9.3	286.2	9.2	287.7	3.6	288.9	1.0
N-CNTs-Fe_1Mn_1 etched	284.3	74.1	284.9	9.8	286.2	10.6	287.6	4.1	289.0	1.4
N-CNTs-Fe_2Mn_1	284.3	78.5	284.9	9.1	286.2	8.7	287.7	2.3	288.8	1.4
N-CNTs-Fe_2Mn_1 etched	284.3	76.5	284.9	9.4	286.2	9.2	287.7	3.3	289.0	1.7

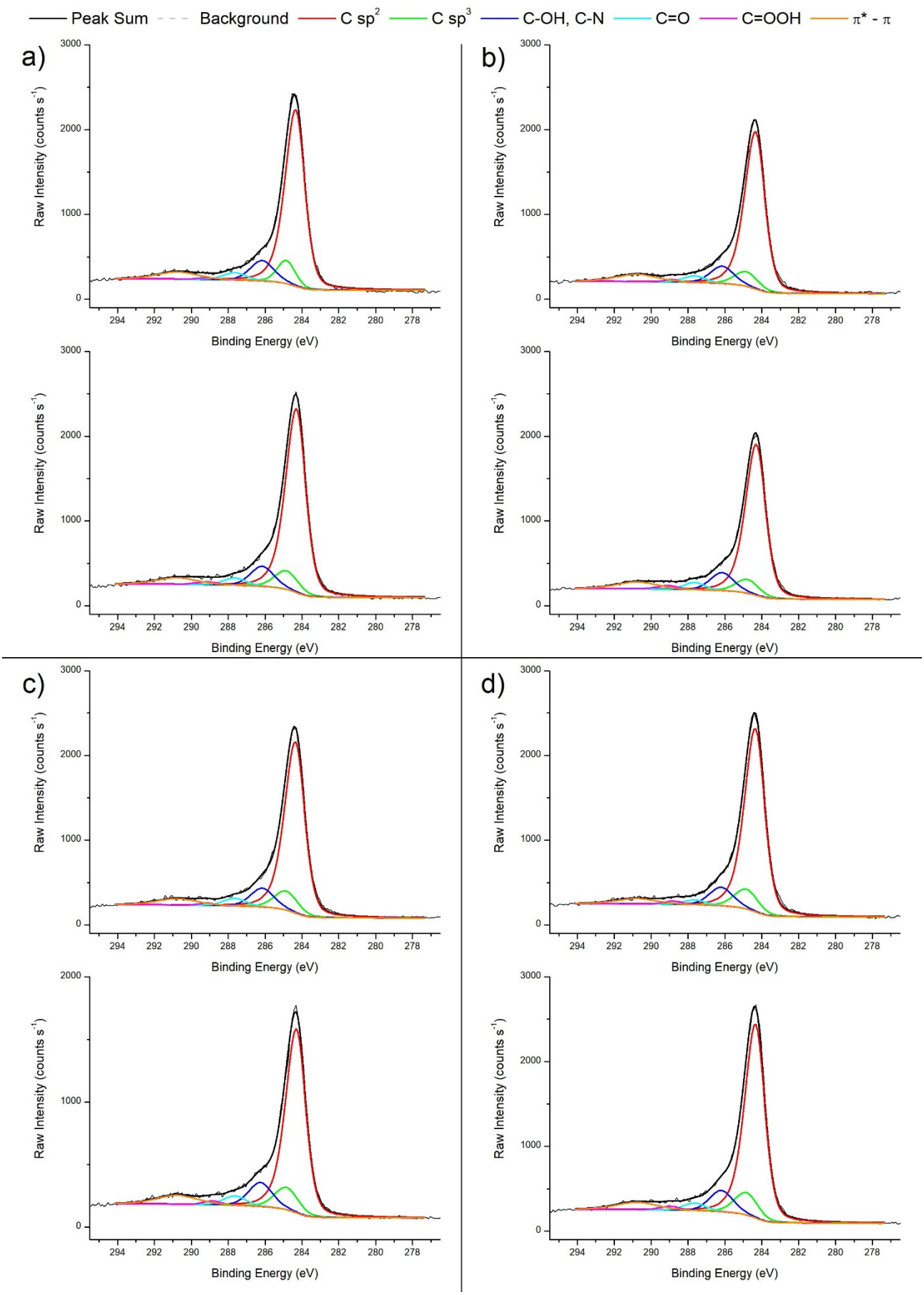

Figure 18. *C1s XPS region, and its deconvolution into chemically shifted components, for materials before (top panels) and after (bottom panels) the etching treatment a) N-CNTs-Fe b) N-CNTs-Mn c) N-CNTs-Fe_1Mn_1 d) N-CNTs-Fe_2Mn_1*

The analysis of the N1s spectrum is carried out by identifying four different nitrogen species: pyridinic, pyrrolic, graphitic, and oxidized nitrogen. The results of the fitting stage of the different materials are then compared considering the BE and the relative presence of the species.

First, the N-doped CNT sample was analyzed, before and after the etching treatment, to determine the effect of the acid treatment (**Figure 19**). For both samples, the N 1s region is separated into four components at 398.2 eV, 399.4 eV, 400.6 eV, and 402.2 eV related to pyridinic, pyrrolic, graphitic, and oxidized N species, respectively. Before the acid treatment, the dominant species was pyridinic N (44.9 at.%), followed by pyrrolic (27.3 at.%), graphitic (20.5 at.%), and oxidized (7.3 at.%). After the treatment, a slight decrease of the pyridinic component and an increase of the other ones is observed. This result can be ascribed to the hydrogenation and protonation of the pyridinic N species during the acid treatment. It is reported that the hydrogenated pyridinic N shows a BE similar to the one of pyrrolic N, while the protonated one has a BE close to the one of the oxidized N [50]. This behavior should be reminded once the comparison between metal-containing samples before and after the etching is performed.

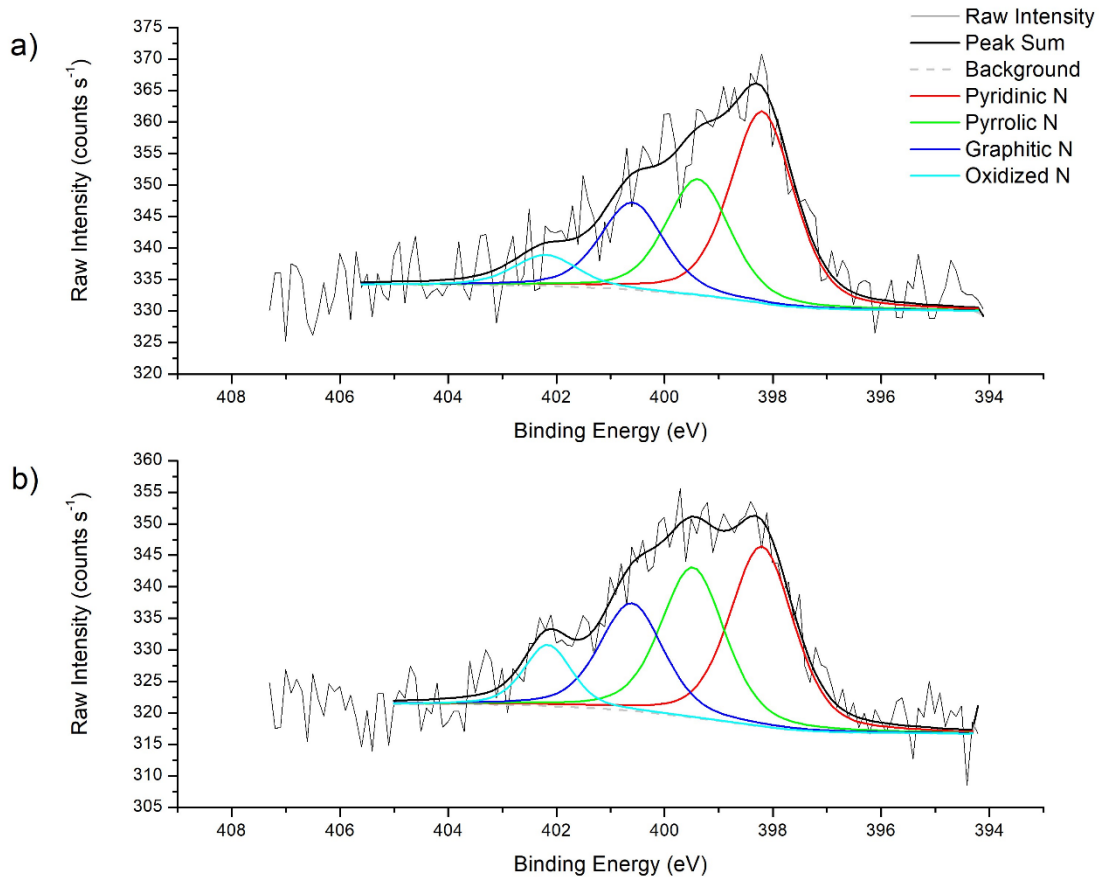

Figure 19. *N 1s XPS region and its deconvolution into chemically shifted components for a) N-CNTs and b) etched N-CNTs*

The N 1s XPS spectra of samples with Fe and Mn, before and after the acid treatment, are reported in **Figure 20**, while the results from the analysis are in **Table 5**. The Fe-N and Mn-N interactions in single metal atom samples are reported at 399.1 eV [51] and 399.8 eV [52], respectively. These components partially overlap with the pyrrolic N species, therefore its identification could be difficult.

To try to detect these moieties the BE and the presence of the pyrrolic N should be compared between the metal-containing samples and the N-CNTs. In fact, the variation of the fitted value of the BE energy of this peak can reveal the addition of a different chemical species.

The N 1s XPS region of the metalated samples was deconvoluted using the same four components described above for the N-CNTs sample. Also for these samples, a slight shift of the pyrrolic-N component is observed after the addition of the metal, which is usually more evident after the acid treatment. This shift is associated with the presence of the metal-N component that overlaps with the pyrrolic N component and that is more evident when only a single metal stabilized by N atoms are present in the sample. However, the hydrogenation of the pyridinic N species cannot be excluded. Therefore, it is difficult to prove the metal-nitrogen interactions from these results.

Table 5. *BE (in eV) and atomic percentage (%) of nitrogen chemical species from the analysis of the N 1s XPS region*

Material	**N pyridinic**		**N pyrrolic**		**N graphitic**		**N oxidized**	
	B.E.	*%*	*B.E.*	*%*	*B.E.*	*%*	*B.E.*	*%*
N-CNTs	398.2	44.9	399.4	27.3	400.6	20.5	402.2	7.3
N-CNTs etched	398.2	37.1	399.5	31.8	400.6	21.9	402.2	9.2
N-CNTs-Fe	398.1	42.9	399.3	30.6	400.7	22.1	402.2	4.4
N-CNTs-Fe etched	398.1	40.6	399.5	37.8	400.8	21.0	403.1	0.6
N-CNTs-Mn	397.9	36.9	399.3	34.8	400.8	19.4	403.3	8.9
N-CNTs-Mn etched	398.0	31.8	399.5	44.2	400.8	16.6	402.0	3.4
N-CNTs-Fe_1Mn_1	398.2	51.5	399.6	27.9	401.1	15.9	403.4	4.7
N-CNTs-Fe_1Mn_1 etched	398.2	39.8	399.4	31.7	400.7	20.5	402.5	8.0
N-CNTs-Fe_2Mn_1	398.2	47.5	399.7	29.2	400.9	18.4	403.2	4.9
N-CNTs-Fe_2Mn_1 etched	398.3	38.4	399.7	35.1	400.8	18.5	402.4	8.0

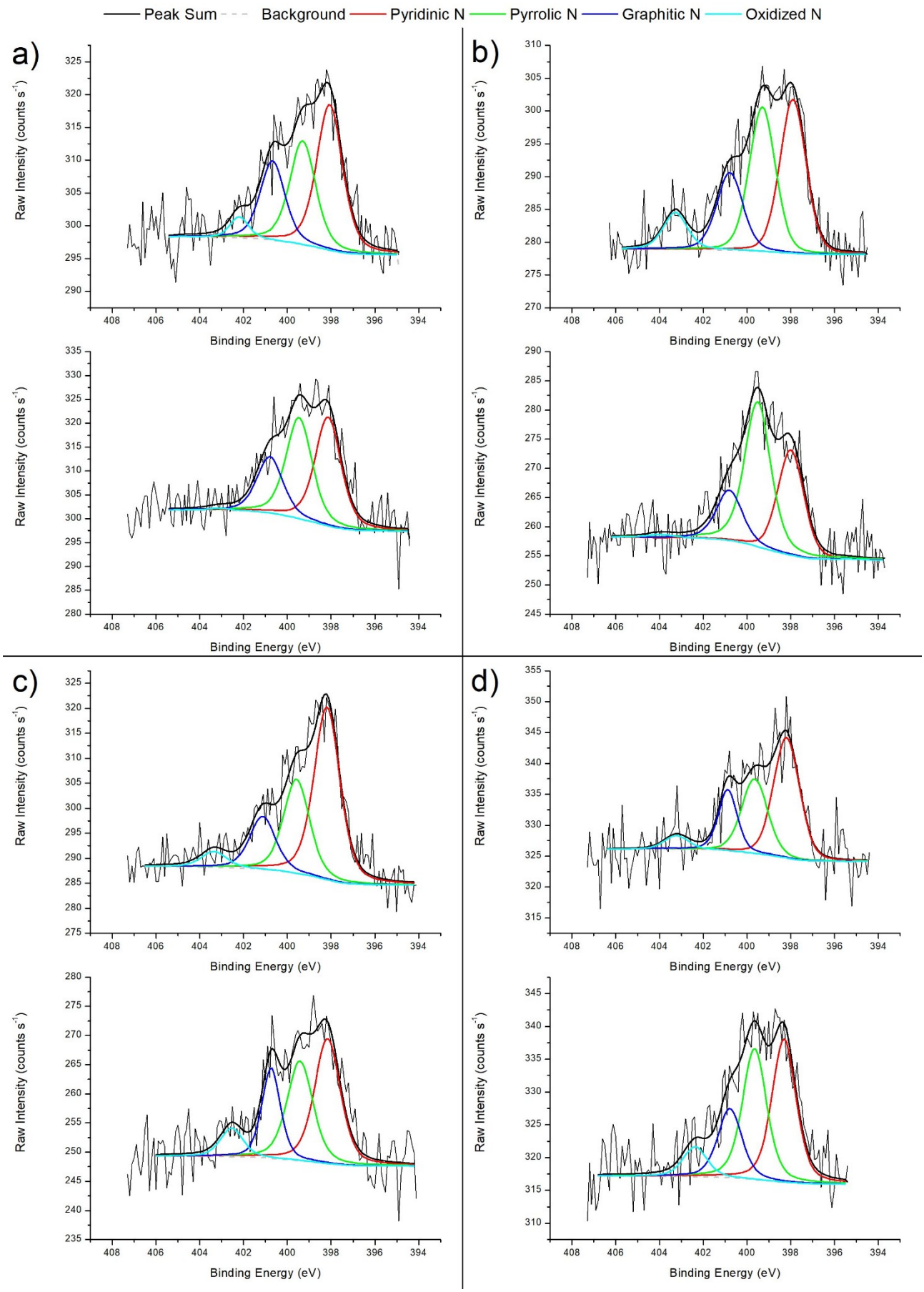

Figure 20. *N1s XPS region, and its deconvolution into chemically shifted components, for materials before (top panels) and after (bottom panels) the etching treatment a) N-CNTs-Fe b) N-CNTs-Mn c) N-CNTs-Fe_1Mn_1 d) N-CNTs-Fe_2Mn_1*

To determine the metal species present at the surface of the catalysts, the Fe 2p and Mn 2p regions were analyzed according the Biesinger's work [53]. Since for a generic metal Me, the spinel structure is given by the coordination of MeO and Me_2O_3, the fit of the 2p regions of Fe and Mn is limited to the 2+ and 3+ oxides and, only in the case of Fe, to metallic Fe(0). Only the $2p_{3/2}$ peak is analyzed since it gives the same chemical information as the $2p_{1/2}$ one.

The analysis of the Fe 2p region (**Figure 21**) shows the presence of Fe(0), FeO, and Fe_2O_3 in all the iron-containing samples, in agreement with the XRD results. The amount of metallic iron is very small in all the samples since XPS is a surface-sensitive technique and, therefore, it is expected to be more sensitive to the oxides present in the surface of the nanoparticles. The effective presence of Fe_2O_3 or Fe_3O_4 or both was determined by considering the relative presence of FeO and Fe_2O_3 components in the fitting stage. Since the spinel structure can also be formed by coordinating MnO instead of FeO, the confirmation of the phases present in the bimetallic samples is given after the analysis of the spectra of Mn2p.

Considering the Fe 2p spectrum for N-CNTs-Fe (**Figure 21a**), the main component is Fe_2O_3, with a lower amount of FeO. Recalling the XRD measurement of this material, we can correctly identify the presence of Fe_2O_3 and Fe_3O_4, formed by the coordination of FeO and Fe_2O_3. Since from the XRD these phases were present in approximately the same amount, the high amount of Fe_2O_3 present can be justified considering the oxidation of the outer layer of alpha-Fe nanoparticles, that are exposed to the atmosphere form Fe_2O_3.

The Mn 2p region for N-CNTs-Mn is represented in **Figure 22a**. For this material, the fit of the signal gives back the contemporary presence of Mn_2O_3 and MnO. This result can be associated with the presence of Mn_3O_4 detected in the XRD. The higher amount of MnO also justifies the presence of this phase as single crystallites in the XRD. No presence of metallic Mn is detected from the XPS.

The analysis of N-CNTs-Fe_1Mn_1 is done considering the Fe2p and Mn2p spectra of this material (**Figures 21b and 22b**). In this case, all the metallic phases identified in the XRD diffractogram are found also in the XPS, with the spinel structures being formed by the coordination of respective 2+ and 3+ oxides. A wide presence of a mixed spinel is excluded since the great amount of MnO detected in the XPS fitting can be directly associated with this phase in the XRD of the material.

N-CNTs-Fe_2Mn_1 XPS signals are portrayed in **Figures 21c and 22c**. The absence of Mn_3O_4 can be easily noticed from the Mn2p spectrum, which is completely described by MnO. Since the XRD pattern of this material does not report the crystalline phase of MnO, we can confirm that manganese monoxide is coordinated by Fe_2O_3 forming the $MnFe_2O_4$ spinel whose presence is asserted in the XRD analysis. The existence of FeO in the fit of Fe2p also hints at the presence of Fe_3O_4, in compliance with the identified crystalline phases in the XRD analysis. The considerations made for N-CNTs-Fe on the amount of metallic Fe and Fe_2O_3 can be repeated also in the case of both bimetallic samples.

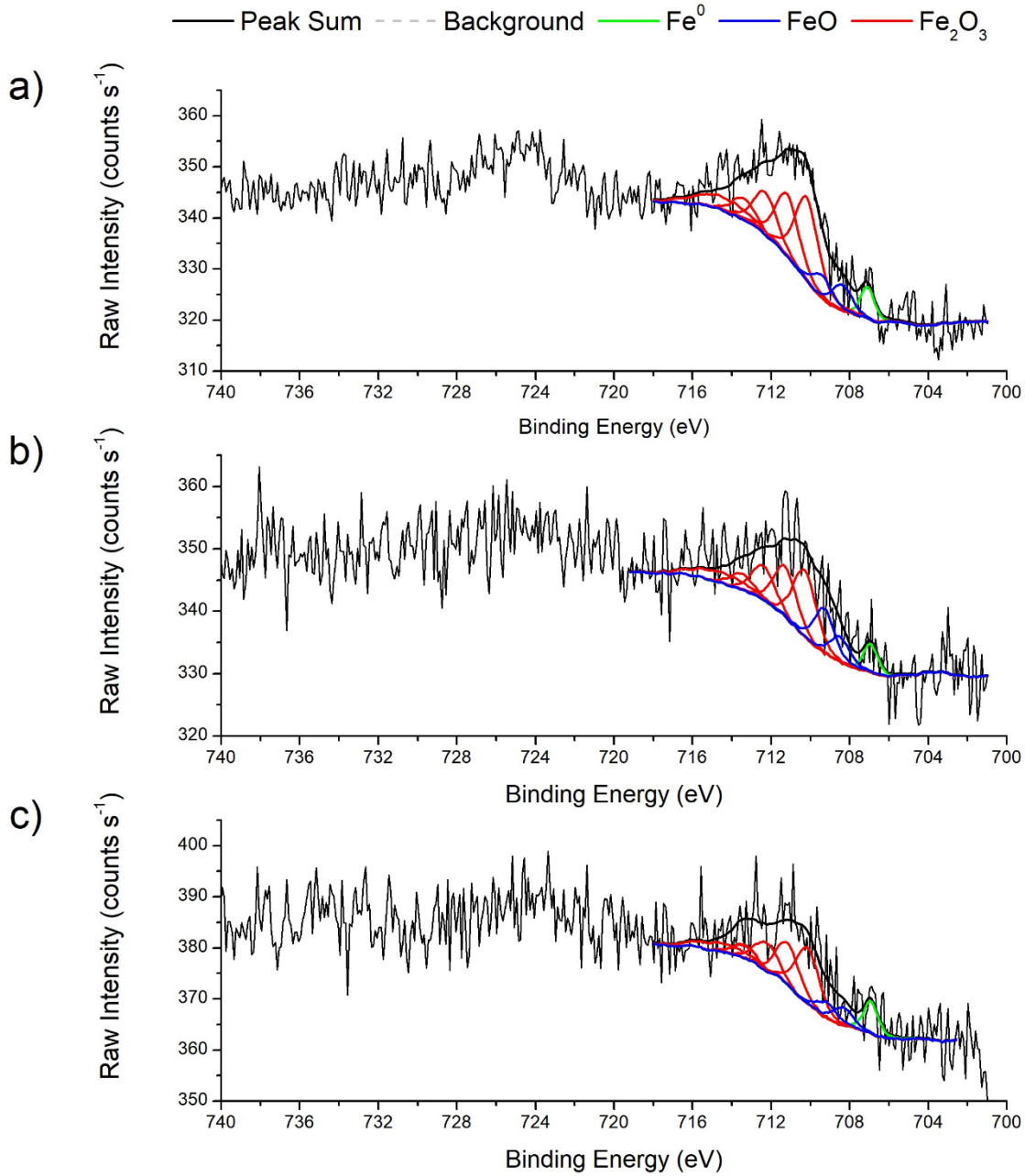

Figure 21. *Fe2p XPS region and its deconvolution in chemically shifted components for a) N-CNTs-Fe b) N-CNTs-Fe_1Mn_1 c) N-CNTs-Fe_2Mn_1 before the etching.*

No peaks related to Fe and Mn can be observed in the XPS measurements carried out on the materials after the etching. Being the metals noticed in etched samples through the TEM/EDX analysis, we can assert that these elements are present below the detection limit of XPS.

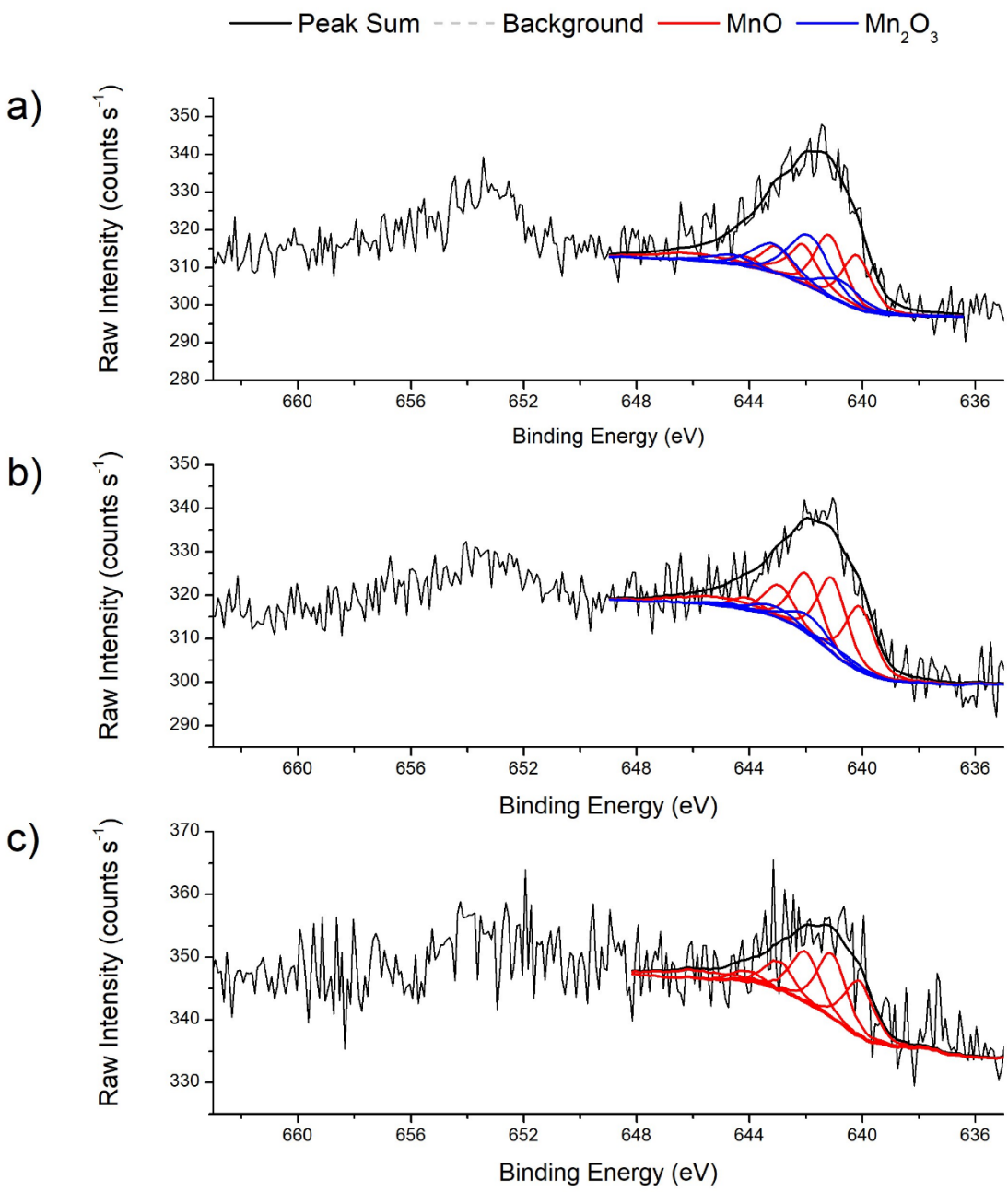

Figure 22. *Mn 2p XPS region and its deconvolution in chemically shifted components a) N-CNTs-Mn b) N-CNTs-Fe_1Mn_1 c) N-CNTs-Fe_2Mn_1 before the etching.*

The surface stoichiometry can be determined considering the area of the XPS regions and the corresponding sensitivity factors. The results presented in **Table 6** show a lower amount of metal than the nominal one. However, the Fe:Mn ratio is maintained in the final materials, 1:1 and 2:1. This suggests that not all the metals included in the synthesis were fixed in the CNTs support or that part of the metals were present inside the CNTs cavity and cannot be detected by XPS.

Table 6. *Quantitative presence of C, O, N, Fe, and Mn in the sample (data in wt.%)*

Material	**C**	**O**	**N**	**Fe**	**Mn**
CNTs hydro	95.1	4.9	-	-	-
N-CNTs	94.4	4.3	1.3	-	-
N-CNTs-Fe	93.1	3.4	1.3	2.1	-
N-CNTs-Fe etched	94.7	4.1	1.2	-	-
N-CNTs-Mn	91.3	4.1	1.9	-	2.7
N-CNTs-Mn etched	93.4	5.1	1.5	-	-
N-CNTs-Fe_1Mn_1	91.5	3.4	1.7	1.7	2.0
N-CNTs-Fe_1Mn_1 etched	92.3	5.9	1.8	-	-
N-CNTs-Fe_2Mn_1	90.6	5.7	0.9	1.8	1.0
N-CNTs-Fe_2Mn_1 etched	94.3	4.5	1.2	-	-

3.2 – Electrochemical characterization

The catalysts prepared in this master thesis were tested as ORR and OER catalysts, reactions that take place during the discharge and charge processes of a metal-air battery at the cathode side. The results are presented and discussed in the following.

3.2.1 – Oxygen Reduction Reaction (ORR)

First, cyclic voltammetries (CVs) in nitrogen-saturated electrolyte were recorded to identify the redox processes associated with the samples. The results are presented in **Figure 23**.

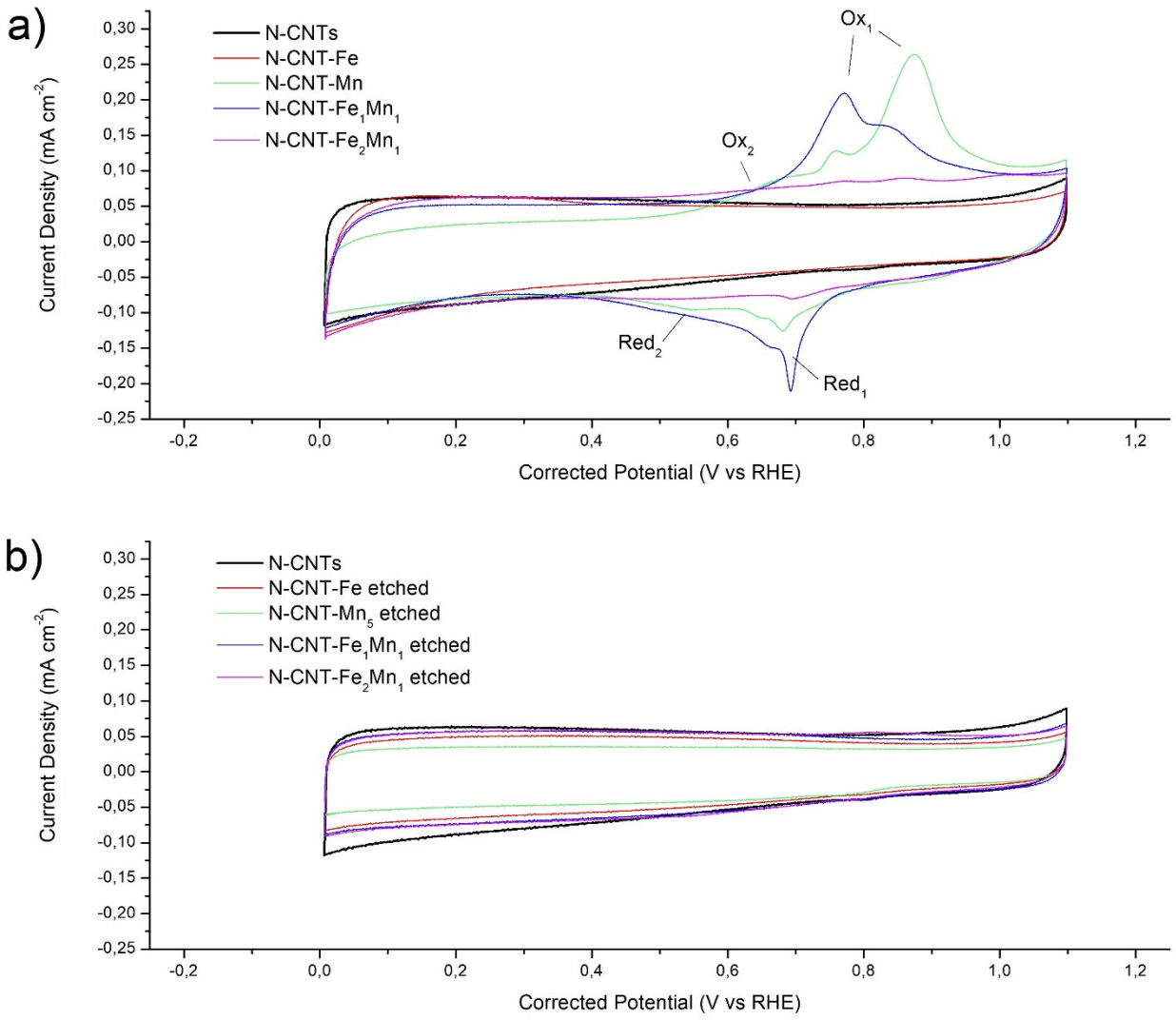

Figure 23. *CVs in nitrogen saturated 0.1 M KOH for materials a) before etching and b) after etching. N-CNTs is reported as reference.*

The CV for N-doped CNTs is characterized by the absence of redox peaks as expected for a carbon material [54]. The voltammograms of materials containing Mn, before the etching step (**Figure 23a**), show different reduction and oxidation peaks. These peaks can be univocally ascribed to Mn since the N-CNT-Fe sample does not show any peak. The different peaks were indexed as Red_1 and Red_2 for the reduction/cathodic peaks, and Ox_1 and Ox_2 for the oxidation/anodic ones. Red_2 and Red_1 peaks are attained at around 0.7 V and 0.5 V vs RHE, respectively, whereas the anodic peaks take place at around 0.65 V (Ox_2) and 0.85 V vs RHE (Ox_1). The current density of the reduction peaks is directly proportional to the amount of Mn, but the ratio of the oxidation peaks varies with the sample composition.

The ongoing reactions associated with each peak can be identified by comparing the obtained results with theoretical studies and literature. Considering first the thermodynamic stability of manganese oxides and hydroxides through the Pourbaix diagram for manganese (**Figure 24**) in the working potential window, we can correlate the different peaks with the transition from one species to another. Starting from 1.1 V vs RHE in the cathodic scanning, the peak Red_1 is associated with the conversion of Mn_2O_3 to Mn_3O_4, and its subsequent reduction to manganese hydroxide in correspondence with the peak Red_2. Once the potential step is inverted the hydroxide is oxidized back to Mn_3O_4 at peak Ox_2 and then converted into Mn_2O_3 at peak Ox_1.

The overall proposed mechanism could be summarized as

$$Mn(OH)_2 \underset{Red_2}{\overset{Ox_2}{\rightleftarrows}} Mn_3O_4 \underset{Red_1}{\overset{Ox_1}{\rightleftarrows}} Mn_2O_3$$

Considering the composition of the metal NPs in the Mn-based samples, it can be concluded that Mn in the $MnFe_2O_4$ spinel is very stable and, therefore, the current densities observed for the N-CNT-Fe_2Mn_1 are very small. The oxidation peak at 0.9 V seems to be related to the presence of Mn_3O_4 since it is the main component in the N-CNT-Mn sample. This suggests that the Mn^{2+} ions in this structure tend to oxidize and form Mn_2O_3.

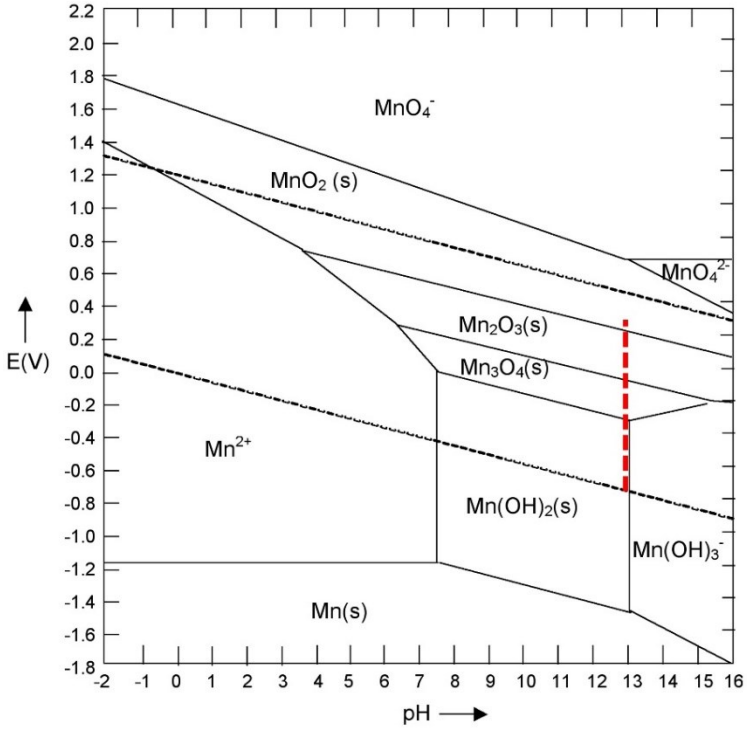

Figure 249. *Pourbaix diagram for Mn. Potential is referenced in V vs SHE. The tested potential range is highlighted in red*

The different subpeaks present in correspondence with Ox_1 refer to the same reaction, the conversion of Mn_3O_4 to Mn_2O_3, though they occur at different potential values. This could be related to the presence of both inner and outer metallic nanoparticles. The CNT-confined manganese oxide particles are facile to form lower oxidation-state species compared to exterior particles, thus the manganese oxides encapsulated inside the CNTs are oxidized at relatively higher potential compared to outer ones [55]. The lower potential subpeaks Ox_1 can then be associated with outer nanoparticles while the higher potential one is associated with inner nanoparticles.

The comparison between samples before and after the etching treatment (**Figure 23b**) underlines that the acid effectively removed exposed nanoparticles from the CNTs, thus eliminating the RedOx peaks of the metals and their oxides. No signals related to SACs or the nanoparticles within the CNTs can be identified.

The CVs in oxygen oxygen-saturated electrolytes are reported in **Figure 25**. In the presence of oxygen, a sharp reduction peak is present at potential values around 0.83 V vs RHE. The comparison of the voltammograms in presence and absence of oxygen allows us to attribute this peak to the reduction of oxygen.

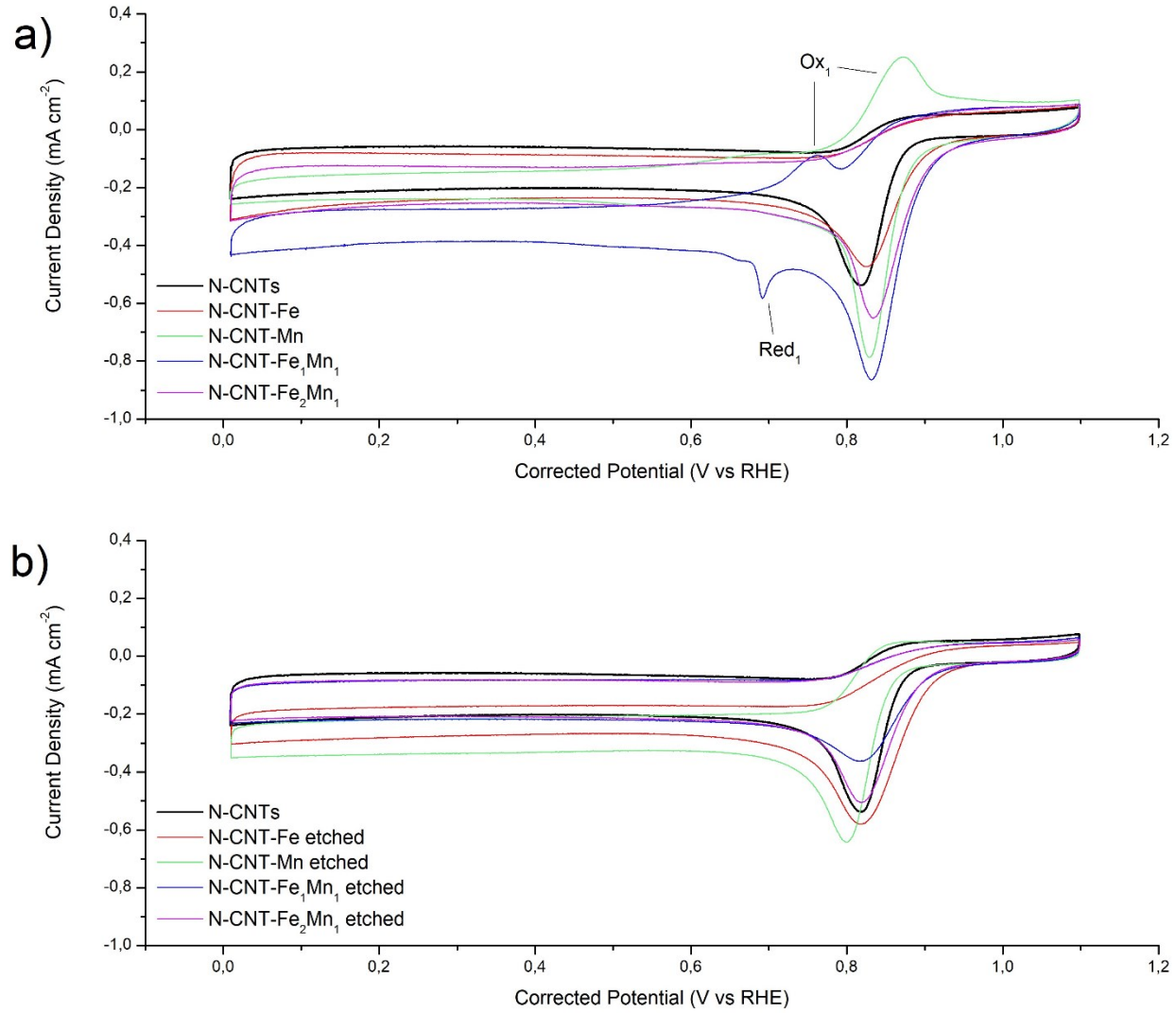

Figure 25. *CVs in oxygen saturated 0.1 M KOH for materials a) before etching and b) after etching. N-CNTs is reported as reference.*

N-CNT-Mn and N-CNT-FeMn samples also show the redox peaks identified above in absence of oxygen. It has to be highlighted that the peaks associated with $Mn(OH)_2$ are not observed in presence of oxygen since it oxidizes the material and, therefore, the formation of the hydroxide is not favored in this media [56].

The performances of the synthesized materials towards ORR were evaluated by comparing the linear sweep voltammetries (LSVs) at 1600 rpm in an oxygen-saturated atmosphere. The LSVs of the disk and ring current densities are reported in **Figure 26**.

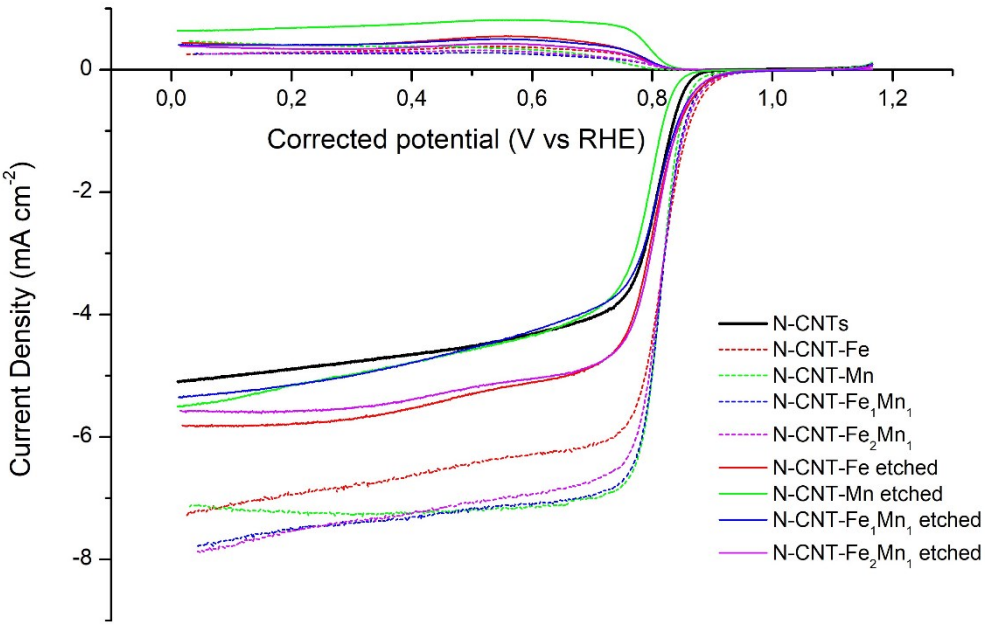

Figure 10. *Ring (positive) and Disk (negative) current densities for the synthesized materials at 1600 rpm in O_2 saturated 0.1 M KOH*

Starting from positive potentials and going towards negative ones, each curve is characterized by a region in which the current is approximately null followed by a rapid increase of the current density once the onset potential is reached. The onset potential is comprised within the interval 0.9 - 0.8 V vs RHE for all the materials. At potentials lower than 0.8 V, the typical plateau is observed and corresponds to the limiting current. In this region, the current is limited by the oxygen diffusion from the bulk solution to the catalyst surface. The entity of the plateau current varies among the different materials, increasing from N-CNTs < N-CNTs-Mn etched = N-CNTs-Fe_1Mn_1 etched < N-CNTs-Fe_2Mn_1 etched = N-CNTs-Fe etched < N-CNTs-Fe < N-CNTs-Mn = N-CNTs-Fe_2Mn_1 = N-CNTs-Fe_1Mn_1. Materials before the acid treatment show better performance with limiting current densities around 8 mA cm^{-2}, while materials after the acid treatment are more similar to N-doped CNTs with limiting current densities up to 6 mA cm^{-2}.

In general, the catalysts before the etching treatment are the most active ones in terms of onset potential and current density. The addition of Mn to the Fe material increases the activity.

As seen in **Figure 27**, the amount of hydrogen peroxide produced by these materials (10%) is much lower than the one produced by N-CNTs (30%), indicating that the metals favor the complete reduction of oxygen to water. As presented in Chapter 1, the oxygen evolution reaction mechanism can follow either the 2-electron or 4-electron pathways. To investigate the tendency of each material towards one or the other mechanism the number of exchanged electrons and the H_2O_2 yield are determined using the correlations between the ring and the disk current. The calculations are made in the plateau region, that is, in the diffusion-controlled region.

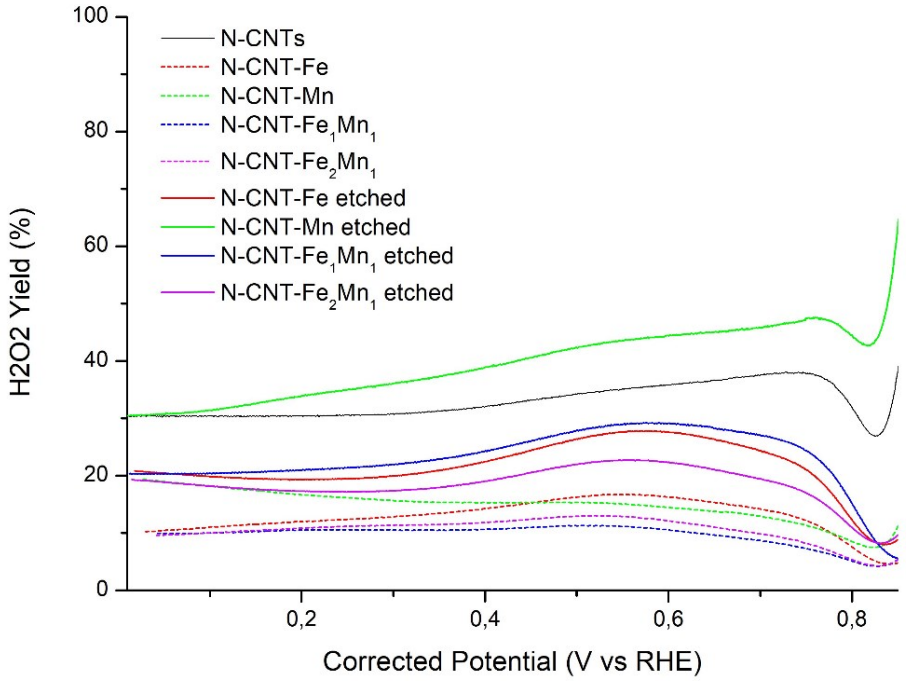

Figure 27. *Hydrogen peroxide yield for LSVs at 1600 rpm in O_2 saturated 0.1 M KOH*

As seen in **Figure 28**, the number of electrons exchanged for these samples is around 3.8, while in the case of N-CNTs, it is around 3.4. In this regard, the bimetallic catalysts are the ones that produce the lowest amount of hydrogen peroxide, suggesting a synergy between the two metals.

After the acid treatment, the current density displayed by the different materials slightly decreases, which can be attributed to the removal of the metal nanoparticles and, therefore, to the decrease of metal sites. The Mn and FeMn catalyst show an LSV very similar to that of N-CNTs. However, the amount of hydrogen peroxide produced by these materials is lower than that obtained with N-CNT, indicating that the single metal sites present in the samples favor the 4-electron mechanism. The two materials with higher content of Fe, N-CNT-Fe, and N-CNT-Fe2Mn, present a better electrochemical performance than the other samples and the substate. In fact, catalysts based on Fe single atoms dispersed in carbon materials have been shown to be very active for the ORR [57].

Comparing the amount of hydrogen peroxide and the number of electrons exchanged for the different materials, it is clear that the metals favor the 4-electron mechanism. The catalysts based on SACs present intermediate behavior between the metal nanoparticles and the substrate as expected, since the amount of metal is much lower and the activity from the substrate is not negligible in this case.

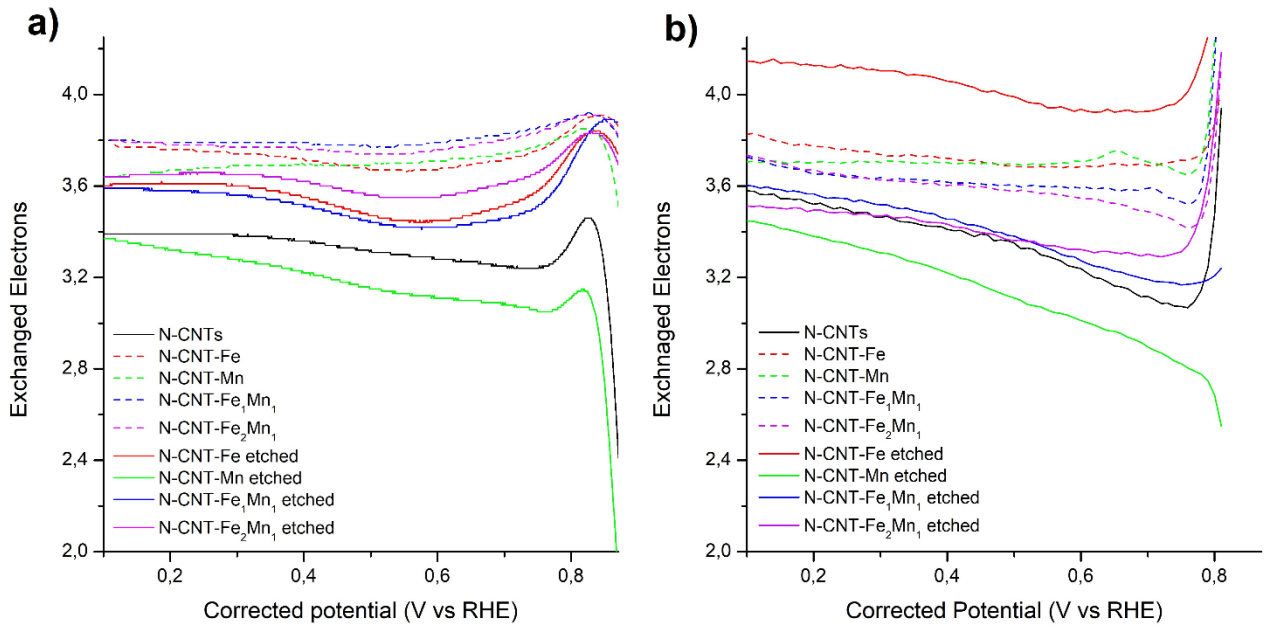

Figure 2811. *Number of electrons exchanged calculated using a) correlation between ring and disk current for LSVs at 1600 rpm in O_2 saturated 0.1 M KOH b) Koutecky-Levich analysis.*

As presented in Chapter 1, ORR in an alkaline environment can be carried out either in the 2-electron or 4-electron pathways. To investigate the tendency of each material towards one or the other mech

The number of exchanged electrons was monitored both through the correlation between the RRDE ring and disk current and the Koutecky-Levich equation. The values of the exchanged electrons determined correlating disk and ring current are comparable with the ones obtained from the Koutecky-Levich analysis, though this procedure tends to overestimate them. This result could be caused by the assumption that the parameters correlating the slope of the linear regression and the electrons exchanged are constant from one LSV to another and among the different materials.

The value of the onset potential of ORR was determined considering the potential at which the second derivative of the LSV curve is minimal. This procedure allowed also us to evaluate the half-wave potential as the potential at which the second derivative is null. The values of the onset potential and the half-wave potential of each material are reported in **Table 7**.

Table 7. *Onset and half-wave potentials, Tafel slope of LSVs at 1600 rpm in O_2 saturated 0.1 M KOH*

Material	**Onset potential** *V vs RHE*	**Half-wave potential** *V vs RHE*	**Tafel slope** *mV/dec*
N-CNTs	0.85	0.81	-47.7
N-CNTs-Fe	0.84	0.82	-79.6
N-CNTs-Fe etched	0.82	0.80	-91.8
N-CNTs-Mn	0.83	0.81	-54.5
N-CNTs-Mn etched	0.82	0.80	-46.1
N-CNTs-Fe_1Mn_1	0.83	0.81	-63.9
N-CNTs-Fe_1Mn_1 etched	0.85	0.81	-75.3
N-CNTs-Fe_2Mn_1	0.84	0.81	-70.1
N-CNTs-Fe_2Mn_1 etched	0.83	0.81	-78.3

The onset potential is often viewed as a simple and easy parameter to give insight into the relative activity of a material [58]. We can then classify the proposed catalysts based on their activity towards ORR using the onset potential as a reference value. In a reduction reaction, higher onset potential values are typical of materials with increased activity whereas lower onset potentials characterize low activity. Literature characterization for Mn oxides nanoparticles show a value of the onset potential of 0.83 V vs RHE but lower current densities are usually evolved [59]. The obtained onset potential values are also compatible with other SACs studies based on iron (0.826 V vs RHE [60]) enforcing the possible presence of this kind of catalytic site in the synthesized material.

To further investigate the activity of the tested materials, the Tafel analysis was carried out. The linear fitting of the potential applied to the electrode and the logarithm of the current density in the kinetic controlled region are presented in **Figure 29** and **Table 7**. The lowest values of the Tafel slope are associated with pristine N-doped CNTs and with etched N-CNTs-Mn. Considering the higher peroxide yield and the lower exchanged electrons number for N-doped CNTs, we can assume that the Tafel slope for this material is caused by the favored kinetics of this material towards the 2-electron pathway. In the case of metal-containing materials, lower Tafel slopes are characteristic of samples in which Mn is present. The atomic fraction of manganese also affects the value of the Tafel slope, which is lower for higher manganese content. Materials after the etching step generally show

a higher Tafel slope compared to the not-etched counterparts. Since the different Tafel slope values lack confidence ranges due to non-reproduced measurements and being the increase in the Tafel slope of limited relevance (approx. 10 mV/dec) we can assume that both the not etched and etched samples have the same rate-determining step.

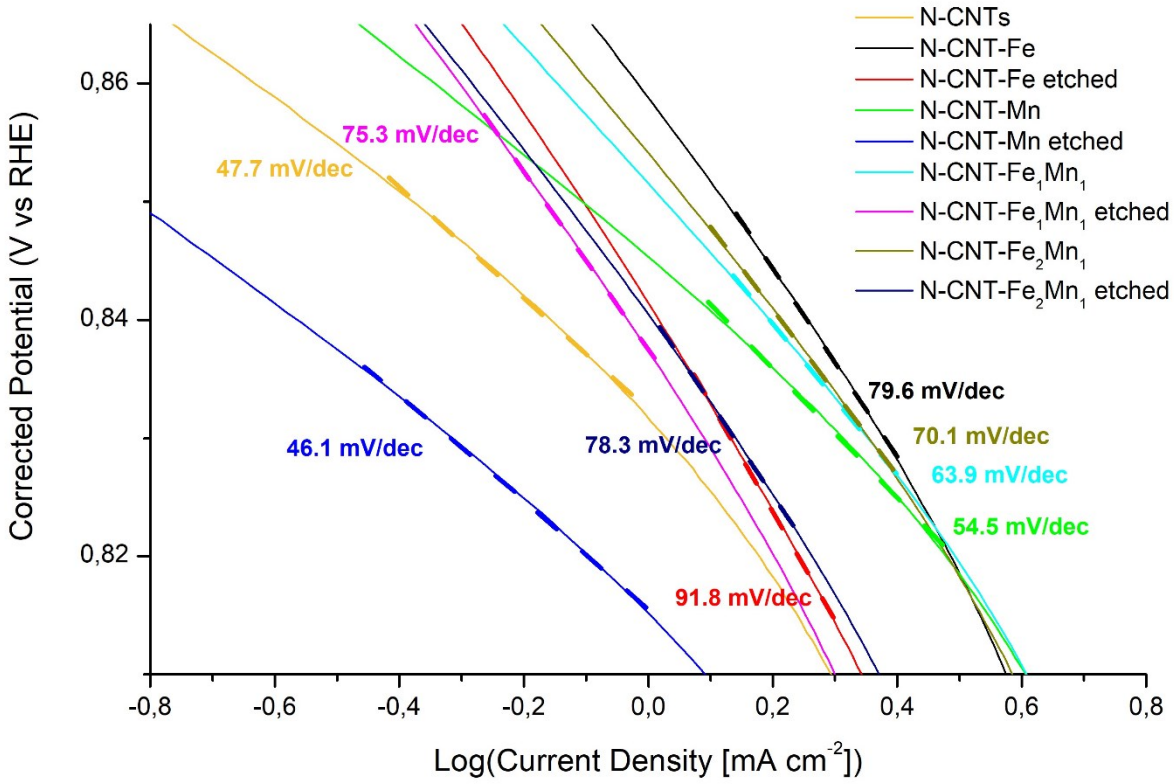

Figure29. *ORR Tafel analysis for LSVs at 1600 rpm in O_2 saturated 0.1 M KOH*

The benchmark for ORR is usually identified in Pt/C. This material is reported to show a Tafel slope of -60 mV/dec in the proximity of the onset, located at 1.07 V vs RHE [61]. The Tafel slope values for the not-etched samples show that these materials have a rate-determining step comparable with Pt. Comparing the obtained results with spinel nanoparticles (Tafel slope of 230 mV/dec [62]), a sensible improvement of the electron transfer can be noted. This effect can be related to the improvement of the electrical conductivity caused by the CNTs.

Considering the values of the limiting current, the onset potential, the number of exchanged electrons, and the Tafel slope, the best material for ORR can be identified in N-CNTs-Mn before the etching. This result agrees with the industrial choice of manganese-based catalysts in the cathodic side of primary Zinc-Air batteries.

3.2.2 – Oxygen Evolution Reaction (OER)

The results of the OER measurement for the tested materials are plotted in **Figure 30**, where stable current density vs potential curves are portrayed.

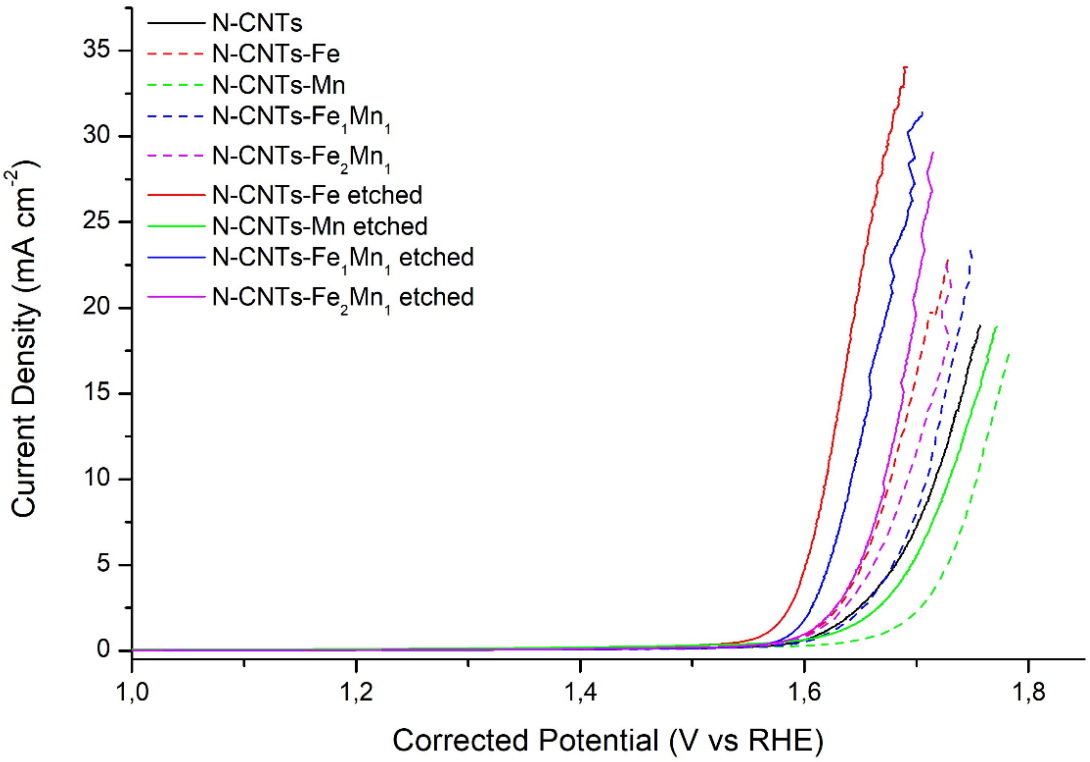

Figure 30. *OER LSVs in O_2 saturated 0.1 M KOH at 1600 rpm*

Since the determination of the onset potential for OER is difficult, the materials are compared considering the potential at which the current density is 10 mA cm^{-2} (E_{10}). These values and the potential difference between the unetched and etched samples (ΔE) are reported in **Table 8**.

It can be first noticed that the materials containing Fe show better performances than N-CNTs while the catalysts with only manganese perform worse. Considering only the samples before the acid treatment, a correlation between the presence of Fe and E_{10} can be noticed. In fact, the E_{10} values of N-CNTs-Fe, N-CNTs-Fe_2Mn_1, and N-CNTs-Fe_1Mn_1 are respectively 0.870, 0.886, and 0.891 V vs RHE, suggesting that a higher Fe content tends to improve the performance of the catalyst before the etching. Since the current density in these three materials is similar, the best activity is associated with the lower value of E_{10}. N-CNTs-Fe is then the best not-etched material.

Table 8. *OER E_{10}, ΔE and Tafel slope for LSVs at 1600 rpm in O_2 saturated 0.1 M KOH*

Material	E_{10} *V vs RHE*	*ΔE* *mV*	**Tafel slope** *mV/dec*
N-CNTs	0.91	-	103.8
N-CNTs-Fe	0.87	-	71.0
N-CNTs-Fe etched	0.80	-70	50.5
N-CNTs-Mn	0.94	-	81.3
N-CNTs-Mn etched	0.91	-30	100.2
N-CNTs-Fe_1Mn_1	0.89	-	87.8
N-CNTs-Fe_1Mn_1 etched	0.83	-60	50.3
N-CNTs-Fe_2Mn_1	0.89	-	84.3
N-CNTs-Fe_2Mn_1 etched	0.86	-30	71.1

After the acid treatments, an increase of the catalytic activity is observed in all cases, in terms of onset potential and current density. This result suggests that single atom catalysts have a higher catalytic activity than the corresponding nanoparticles. Also for the SAC-based catalysts, the best performance is obtained with the sample containing only Fe. However, since it has not been possible to do the compositional analysis, it is difficult to compare the performance of these materials in terms of type and amount of metals.

To analyze the kinetics of the reaction, the Tafel slope of each material is determined. The obtained values are reported in **Figure 31** and **Table 8**.

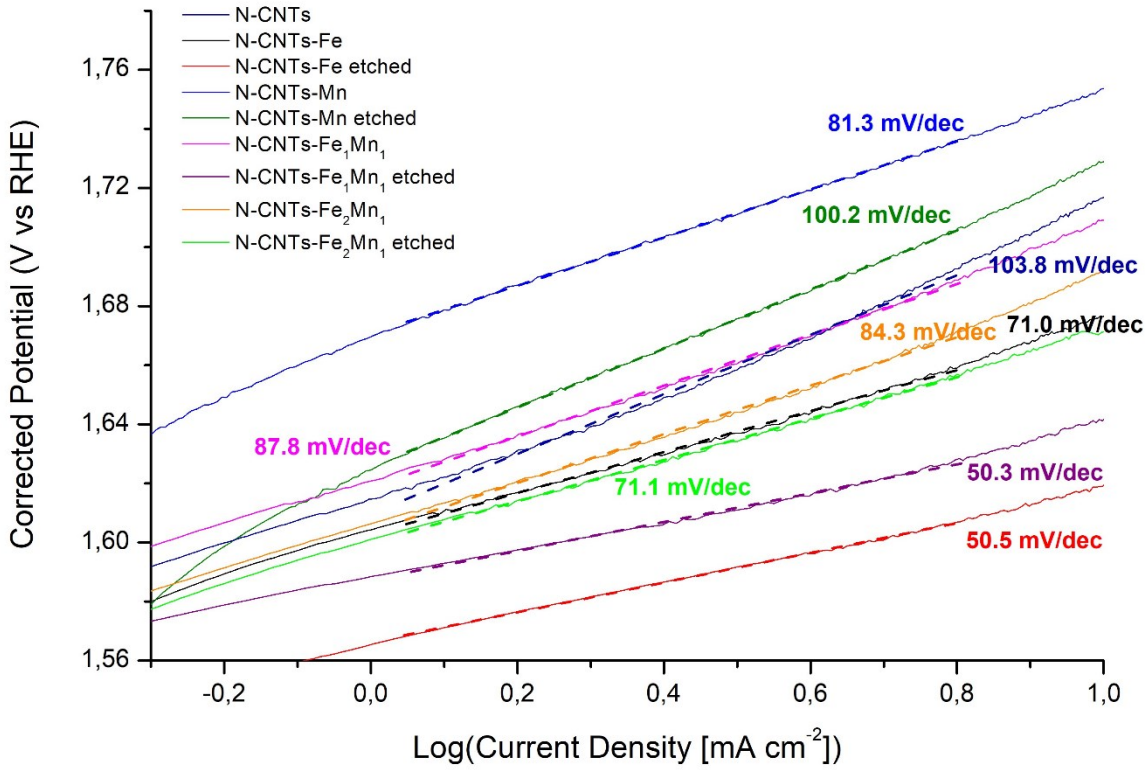

Figure 3112. *OER Tafel analysis for LSVs at 1600 rpm in O_2 saturated 0.1 M KOH*

The results of the Tafel analysis for N-CNTs-Mn show that the rate determining step for this material is different from the N-CNTs (Tafel slope 81.3 vs 103.8 mV/dec). Once the material is etched, though the current density is higher and E_{10} is lower, the electron transfer is worsened and becomes comparable with the base material. The same cannot be said for the Fe-containing samples, where a noticeable decrease of the Tafel slope occurs between the not-etched and the etched samples. These samples already show a Tafel slope consistently lower than the base material before the removal of nanoparticles. The exposure to the acid further lowers the Tafel slope, which reaches values of 50.5 and 50.3 mV/dec respectively for N-CNTs-Fe and N-CNTs-Fe_1Mn_1 etched samples.

The reduction of the Tafel slope of the material after the etching can be explained by considering the correlation between its value and the rate determining step of the reaction. As previously stated, OER is a four-electron process. Since this reaction presents some intermediates, the four electrons may not be transferred simultaneously. For the occurrence of all the steps of OER, associated with a Tafel slope of 30 - 40 mV/dec, it is predicted that the active sites must be much closer to one another [63]. Catalysts with Tafel slopes above 40 mV/dec and below 90 mV/dec, as in the present

case, are considered to have some sites that are close enough to follow the four-electron path and some are not, being limited by intermediate reactions. Lower Tafel slope N-CNTs-Fe and N-CNTs-Fe_1Mn_1 etched samples can then be associated with a different rate determining step compared to the NPs containing materials. The presence of single-atom or dual-atom catalytic sites is not excluded either. Literature data report Tafel slopes for the considered transition metal SACs around 50 - 60 mV/dec [64].

Conclusions

In this Master thesis, single- and dual-metal catalysts (SAC, DAC) based on iron and manganese stabilized in N-doped CNTs have been prepared by a thermal method. For this aim, metal salts precursor, melamine and carbon nanotubes were mixed and subjected to a thermal treatment in inert atmosphere at 800°C for 2 h. Samples obtained presented a high amount of metal-based nanoparticles that were eliminated by an acid treatment in 1M H_2SO_4 at 100°C to obtain the corresponding SACs and DACs materials.

All the samples prepared were characterized by different physicochemical techniques in order to determine their morphological and chemical properties, that then were related to their electrochemical performance toward the oxygen reduction and evolution reactions (ORR, OER).

The morphology of the catalysts was studied by transmission electron microscopy (TEM). In this way, the presence of metal nanoparticles after the thermal treatment and their removal after the acid treatment were confirmed. From the TEM images, it was also possible to observe the presence of nanoparticles both at the surface and inside the cavity of the CNTs, as well as the presence of sulfur contamination in samples before the etching, probably incorporated into the CNTs structure during the H_2SO_4 treatment. From energy disperse X-ray spectroscopy (TEM-EDX) it was possible to confirm that the NPs found within the nanotubes were of the same nature as the ones decorating their surface. Unfortunately, it was not possible to determine the presence of SACs and DACs in the samples by TEM images since the instrument used for the measurements was not an aberration corrected TEM.

The nature of the metal nanoparticles was determined by X-ray diffraction (XRD). The phases identified consisted of Fe and Mn alloys and oxides, with the presence of mixed oxides in samples where both metals were present. Samples containing only Fe were characterized by the presence of metallic Fe, Fe_2O_3, and Fe_3O_4 nanoparticles. In materials with only manganese the nanoparticles were composed of metallic Mn, MnO and Mn_3O_4. In the for a Fe:Mn atomic ratio 1:1 the phases identified consisted of metallic Fe/Mn, MnO, Mn_3O_4 whereas with a increasing the ratio to 2:1 the nanoparticles were preferentially composed of $MnFe_2O_4$.

The chemical nature of the metal nanoparticles, as well as the chemical species present at the surface of the materials was confirmed by X-ray photoemission spectroscopy (XPS). These results confirmed the formation of hydrophilic groups on the surface of MWCNTs during the initial functionalization of the CNTs, as well as the nitrogen doping during the thermal treatment. The main

N species obtained were pyridinic one, but also the presence of pyrrolic and graphitic N was observed, as well as a small amount of nitrogen oxide. Metalated samples contained the same N species with slight differences in the at.%. The deconvolution of the XPS regions in chemically shifted peaks allowed us to identify the main type of bonds and moieties present in the samples, confirming the metal and metal oxide phases previously identified by XRD.

All the catalysts were tested toward the ORR and OER. The results of the evaluation of the ORR activity pointed out that samples before the etching show higher limiting current, lower hydrogen peroxide yield, and higher exchanged electrons compared to N-CNTs and their corresponding leached samples. This result is associated with the prevalence of the 4-electron mechanism in samples containing NPs. The evaluation of the number of exchanged electrons was achieved both by using the correlation between ring and disk current in the RRDE and performing the Koutecky-Levich analysis, giving comparable values between the two different techniques. The evaluation of the onset and half-wave potential was carried out in an unbiased way by studying the second derivative of LSVs. The obtained values for different materials were very similar with values around 0.83 V vs RHE. Compared to conventional noble metal catalysts (Pt), the synthesized materials show a higher overpotential. However, it has to be considered that the cost of the proposed materials is much lower and a compromise between activity and costs has to be achieved. Compared with other transition metal-based catalysts reported in the literature the obtained results for the onset potential are in line with transition metal oxides results while higher current densities are measured. The kinetics of the reaction was studied determining the value of the Tafel slope for each material. The obtained values showed that the atomic fraction of manganese affects the value of the Tafel slope, which is lower for higher manganese content. Materials after the etching step generally show a higher Tafel slope compared to the not-etched counterparts. The comparison of the Tafel slope with Pt shows that not-etched samples have a rate-determining step comparable with Pt. Considering the values of the limiting current, the onset potential, the number of exchanged electrons, and the Tafel slope, the best material for ORR of the synthesized ones can be identified in N-CNTs-Mn before the etching. This result agrees with the industrial choice of manganese-based catalysts in the cathodic side of primary Zinc-Air batteries.

Regarding the OER, before the etching treatment, materials containing iron perform better than those without it (N-CNTs and N-CNT-Mn). The evolved current is proportional to the amount of Fe present. An increase of the catalytic activity was observed for all the materials after the acid treatment. Moreover, the value of the potential at 10 mA cm^{-2} is anticipated in samples after the

etching. The decrease of this potential after acid treatment varies for Fe-containing materials. The kinetics of the reaction was determined by calculating the Tafel slope for each material. The results showed that materials after the etching generally show a lower Tafel slope than before the acid treatment. The obtained Tafel slope for N-CNTs-Fe and N-CNTs-Fe_1Mn_1 etched samples were 50.5 and 50.3 mV/dec, respectively, very similar to literature Tafel slope for transition metal SACs (50 - 60 mV/dec).

The presence of SACs and DACs could not be demonstrated through the performed characterization. To solve this issue samples should be characterized using aberration-corrected TEM, which allows higher magnifications and atomic resolution, or extended X-ray absorption fine structure spectroscopy (EXAFS). These techniques are commonly employed in the characterization of single atom-containing materials.

Further analysis should be focused on the quantification of the metals in the synthesized samples by inductively coupled plasma – optical emission spectroscopy (ICP-OES). The availability of these data could give additional insights into the amount of metal coordinated by the CNTs during the synthesis and would allow a more realistic account of the electrochemical performance of the materials, which could be compared on the base of the metal content instead of limiting the normalization on the value of the geometrical area of the electrode.

Riassunto esteso

In questo riassunto è presentata estensivamente la procedura di sintesi utilizzata e sono riportati i principali risultati e le conclusioni relative a questo lavoro di tesi.

Sintesi

I nanotubi di carbonio multiparete (MWCNT) sono stati inizialmente sottoposti a un trattamento di funzionalizzazione per creare gruppi idrofili superficiali. A tale scopo, 200 mg di MWCNT sono stati dispersi in una soluzione da 52 mL di H_2SO_4 e HNO_3 concentrati in un rapporto volumetrico di 3:1 in un pallone volumetrico e sonicati per 30 minuti. Successivamente, la miscela è stata lasciata sotto agitazione a temperatura ambiente per 24 ore. Dopo filtrazione e vari lavaggi in acqua milli-Q fino a neutralizzazione, i MWCNT sono stati nuovamente posti in agitazione per 24 ore in 25 mL di HNO_3 5M. Dopo filtrazione e lavaggio con acqua milli-Q, i MWCNT sono stati dispersi in acqua milli-Q. La miscela è stata quindi congelata e l'acqua è stata rimossa mediante liofilizzazione. I nanotubi di carbonio funzionalizzati risultanti sono stati etichettati come *CNThydro* e impiegati nella sintesi di tutti i materiali studiati.

Per sintetizzare i catalizzatori analizzati, 20 mg di *CNThydro* sono stati dispersi insieme a 63 mg di melammina e una quantità variabile di soluzione contenente metallo in 50 mL di acqua milli-Q e sonicati per almeno 30 minuti. La miscela è stata poi lasciata sotto agitazione per la notte (almeno 15 ore) a 50 °C e nuovamente sonicata per 2 ore. Successivamente, l'acqua è stata rimossa mediante liofilizzazione per preservare l'elevata area superficiale del materiale originale. La polvere secca è stata posta in una barchetta di allumina e sottoposta a un trattamento ad alta temperatura in atmosfera di azoto. Tale trattamento consiste in un riscaldamento fino a 400 °C a 2°C/min, 30 minuti a temperatura costante di 400°C, seguito da una seconda rampa di riscaldamento a 5°C/min fino a 800 °C e mantenimento per 2 ore alla stessa temperatura.

La polvere risultante è stata quindi trattata con una soluzione di H_2SO_4 1 M a 100°C sotto agitazione per rimuovere le eventuali nanoparticelle formate durante il processo ad alta temperatura. La caratterizzazione fisico-chimica ed elettrochimica è stata effettuata su campioni sia prima che dopo il trattamento acido.

Sono state sintetizzate cinque diverse categorie di catalizzatori a base di nanotubi di carbonio, a seconda della quantità di ferro e manganese nel campione. Un campione senza alcun metallo è stato sintetizzato come controllo. Il contenuto di metallo nel campione, se presente, è stato fissato a 1

mg, ovvero al 5% in peso del contenuto di nanotubi di carbonio. I campioni sono stati denominati considerando i rapporti atomici tra i metalli presenti nel materiale. Un riepilogo del contenuto di metallo e la designazione di ciascun materiale non disgregato sono riportati nella **Tabella 2**.

Caratterizzazione

I catalizzatori a base di CNT sintetizzati sono stati caratterizzati mediante Diffrazione di raggi X (XRD), Microscopia elettronica a trasmissione (TEM) e Spettroscopia fotoelettronica a raggi X (XPS).

La caratterizzazione elettrochimica è stata effettuata preparando un inchiostro elettrochimico per ciascun materiale. L'inchiostro è stato preparato disperdendo 1 mg del catalizzatore testato in 200 µL di acqua Milli-Q, 50 µL di etanolo e 3 µL di soluzione di Nafion (5%) e sonicando per almeno 30 minuti. L'inchiostro prodotto è stato quindi depositato sul carbonio vetroso di un elettrodo a disco rotante (diametro 3 mm) e di un elettrodo a disco ad anello rotante (diametro 5 mm) per ottenere un film omogeneo. La quantità del catalizzatore depositata è stata di 0,56 mg cm^{-2} in entrambi i casi.

Le misurazioni elettrochimiche sono state effettuate in una cella elettrochimica a tre elettrodi in soluzione KOH 0,1 M in una cella di polipropilene. Come elettrodo di lavoro è stato utilizzato un carbonio vetroso rivestito con l'inchiostro del catalizzatore, mentre un elettrodo Hg/HgO e un'asta di grafite sono stati utilizzati rispettivamente come elettrodo di riferimento e controelettrodo.

La reazione di evoluzione di ossigeno (OER) è stata effettuata utilizzando una punta RDE, saturando l'elettrolita in ossigeno e registrando successive voltammetrie cicliche (CV) a una velocità di rotazione fissa di 1600 rpm. Le CV hanno acquisito una singola scansione da 0,1 V vs ref. a 1,0 V vs ref con un passo di 5 mV sec^{-1} e sono state ripetute fino a quando le curve i-V sono risultate stabili.

La reazione di riduzione dell'ossigeno (ORR) è stata effettuata utilizzando una punta RRDE. L'elettrolita è stato prima saturato in azoto. Si è quindi proceduto alla stabilizzazione del materiale acquisendo 50 CV nell'intervallo da -0,86 - -0,17 V vs ref a 200 mV sec^{-1} a 1600 rpm. Sono state poi eseguite tre CV nell'intervallo da -0,86 - 0,23 V vs ref a 5 mV sec^{-1} in configurazione statica. La stessa misura CV è stata poi ripetuta dopo aver saturato l'elettrolita in ossigeno. L'ORR è stata investigata eseguendo LSV a 200, 400, 600, 900, 1200, 1600, 2000, 2200 e 2500 giri al minuto da 0,3 V vs ref a -0,9 V vs ref a 5 mV sec^{-1}. Queste misurazioni sono state eseguite senza un ordine particolare. Tra due LSV consecutive, è stato fatto gorgogliare ossigeno nella soluzione per 60 secondi per garantire la saturazione dell'elettrolita. Durante le LSV, il potenziale all'anello di Pt è stato fissato a 0,55 V vs ref.

Risultati

La morfologia dei catalizzatori è stata studiata mediante microscopia elettronica a trasmissione (TEM). In questo modo, è stata confermata la presenza di nanoparticelle metalliche dopo il trattamento termico e la loro rimozione dopo il trattamento acido. Dalle immagini TEM, è stato inoltre possibile osservare la presenza di nanoparticelle sia sulla superficie che all'interno della cavità dei CNT, nonché la presenza di contaminazione di zolfo nei campioni prima del trattamento acido, probabilmente incorporata nella struttura dei CNT durante il trattamento con H_2SO_4. Dalla spettroscopia a raggi X dispersiva di energia (TEM-EDX) è stato possibile confermare che le NP trovate all'interno dei nanotubi erano della stessa natura di quelle che ne decoravano la superficie. Purtroppo, non è stato possibile determinare la presenza di SAC e DAC nei campioni mediante immagini TEM poiché lo strumento utilizzato per le misure non era un TEM corretto per l'aberrazione.

La natura delle nanoparticelle metalliche è stata determinata mediante diffrazione di raggi X (XRD). Le fasi identificate consistevano in leghe e ossidi di Fe e Mn, con presenza di ossidi misti nei campioni dove erano presenti entrambi i metalli. I campioni contenenti solo Fe erano caratterizzati dalla presenza di nanoparticelle metalliche di Fe, Fe_2O_3 e Fe_3O_4. Nei materiali con solo manganese le nanoparticelle erano composte da Mn metallico, MnO e Mn_3O_4. Nel caso di un rapporto atomico Fe:Mn 1:1 le fasi identificate consistevano in Fe/Mn metallico, MnO, Mn_3O_4 mentre aumentando il rapporto a 2:1 le nanoparticelle erano composte preferenzialmente da $MnFe_2O_4$.

La natura chimica delle nanoparticelle metalliche, così come le specie chimiche presenti sulla superficie dei materiali, è stata confermata dalla spettroscopia a fotoemissione di raggi X (XPS). Questi risultati hanno confermato la formazione di gruppi idrofili sulla superficie dei MWCNT durante la funzionalizzazione iniziale dei CNT, nonché il dopaggio con azoto durante il trattamento termico. Le principali specie di N ottenute sono quella piridinica, ma si è osservata anche la presenza di N pirrolico e grafitico, nonché una piccola quantità di ossido di azoto. I campioni metallizzati contengono le stesse specie di N con lievi differenze nella percentuale atomica. La deconvoluzione delle regioni XPS ha permesso di identificare il tipo principale di legami e gruppi funzionali presenti nei campioni, confermando le fasi metalliche e degli ossidi metallici precedentemente identificate mediante XRD.

Tutti i catalizzatori sono stati testati per ORR e OER. I risultati della valutazione dell'attività ORR hanno evidenziato che i campioni prima del trattamento acido presentano una corrente limite più

alta, una resa di perossido di idrogeno inferiore e un maggior numero di elettroni scambiati rispetto agli N-CNT e ai loro corrispondenti campioni trattati. Questo risultato è associato alla prevalenza del meccanismo a 4 elettroni nei campioni contenenti nanoparticelle (NP). La valutazione del numero di elettroni scambiati è stata ottenuta sia utilizzando la correlazione tra corrente di anello e disco nell'elettrodo a rotante ad anello e disco (RRDE) sia eseguendo l'analisi di Koutecky-Levich, ottenendo valori confrontabili tra le due tecniche. La valutazione del potenziale di *onset* e di *half-wave* è stata effettuata in modo imparziale studiando la derivata seconda delle curve LSV (curve voltammetriche a scansione lineare). I valori ottenuti per diversi materiali sono stati molto simili con valori intorno a 0.83 V vs RHE (Potenziale di Riferimento dell'Idrogeno). Rispetto ai catalizzatori convenzionali a base di metalli nobili (Pt), i materiali sintetizzati mostrano un sovra potenziale maggiore. Tuttavia, va tenuto conto che il costo dei materiali proposti è molto inferiore ed è necessario raggiungere un compromesso tra attività e costi. Confrontando i risultati con altri catalizzatori a base di metalli di transizione riportati in letteratura, i valori ottenuti per il potenziale di inizio sono in linea con ossidi di metalli di transizione, mentre vengono misurate densità di corrente più elevate. La cinetica della reazione è stata studiata determinando il valore della pendenza di Tafel per ciascun materiale. I valori ottenuti hanno mostrato che la frazione atomica di manganese influenza il valore della pendenza di Tafel, che è inferiore per un contenuto di manganese più elevato. I materiali dopo il trattamento acido mostrano generalmente una pendenza di Tafel più alta rispetto alle controparti non trattate. Il confronto della pendenza di Tafel con Pt mostra che i campioni non trattati hanno un *rate-detemining step* paragonabile a Pt. Considerando i valori della corrente limite, il potenziale di inizio, il numero di elettroni scambiati e la pendenza di Tafel, il miglior materiale per ORR tra quelli sintetizzati può essere identificato in N-CNT-Mn prima del trattamento acido. Questo risultato concorda con la scelta industriale dei catalizzatori a base di manganese nel lato catodico delle batterie primarie Zinco-Aria.

Riguardo all'OER, prima del trattamento acido, i materiali contenenti ferro (Fe) performano meglio di quelli senza (N-CNT e N-CNT-Mn). La corrente sviluppata è proporzionale alla quantità di Fe presente. Si è osservato un aumento dell'attività catalitica per tutti i materiali dopo il trattamento acido. Inoltre, il valore del potenziale a 10 mA cm^{-2} è anticipato nei campioni senza nanoparticelle. La diminuzione di questo potenziale dopo il trattamento acido varia per i materiali contenenti Fe. La cinetica della reazione è stata determinata calcolando la pendenza di Tafel per ciascun materiale. I risultati hanno mostrato che i materiali dopo il trattamento acido generalmente presentano una pendenza di Tafel inferiore rispetto a prima del trattamento acido. La pendenza di Tafel ottenuta

per i campioni N-CNT-Fe e N-CNT-Fe_1Mn_1 dopo la rimozione delle NP è risultata rispettivamente di 50,5 e 50,3 mV/dec, valori molto simili alla pendenza di Tafel riportata in letteratura per i catalizzatori SAC (*Single Atom Catalyst*) a base di metalli di transizione (50-60 mV/dec).

La presenza di SAC e DAC (*Dual Atom Catalyst*) non è stata dimostrata attraverso le caratterizzazioni effettuate. Per risolvere questo problema, i campioni dovrebbero essere analizzati utilizzando TEM ad alta risoluzione con correzione dell'aberrazione o spettroscopia EXAFS (Spettroscopia di Assorbimento ai Raggi X ad Alta Risoluzione). Queste tecniche sono comunemente impiegate nella caratterizzazione di materiali contenenti singoli atomi.

Ulteriori analisi dovrebbero essere focalizzate sulla quantificazione dei metalli nei campioni sintetizzati mediante spettroscopia ICP-OES (*Inductively Coupled Plasma - Optical Emission Spectroscopy*). La disponibilità di questi dati potrebbe fornire informazioni aggiuntive sulla quantità di metallo coordinato con i CNT durante la sintesi e consentirebbe una valutazione più realistica delle prestazioni elettrochimiche dei materiali, che potrebbero essere confrontate sulla base del contenuto di metallo invece di limitare la normalizzazione sul valore dell'area geometrica dell'elettrodo.

References

1. Larcher, D., & Tarascon, J.-M. (2014). *Towards greener and more sustainable batteries for electrical energy storage*. In Nature Chemistry (Vol. 7, Issue 1, pp. 19–29). Springer Science and Business Media LLC. https://doi.org/10.1038/nchem.2085
2. IEA (2024), *Electricity 2024*, IEA, Paris https://www.iea.org/reports/electricity-2024, Licence: CC BY 4.0
3. Peterson, K. W., Constantinos A Balaras, Drury B Crawley, Hedrick, R., Nesler, C., Tomlinson, E. K., & Torcellini, P. (2022). *ASHRAE Position Document on Building Decarbonization*. Unpublished. https://doi.org/10.13140/RG.2.2.32640.71689
4. Kumi, E. N. (2023). E*nergy storage technologies*. In Pumped Hydro Energy Storage for Hybrid Systems (pp. 1–21). Elsevier. https://doi.org/10.1016/b978-0-12-818853-8.00002-9
5. Yang, Z., Zhang, J., Kintner-Meyer, M. C. W., Lu, X., Choi, D., Lemmon, J. P., & Liu, J. (2011). *Electrochemical Energy Storage for Green Grid*. In Chemical Reviews (Vol. 111, Issue 5, pp. 3577–3613). American Chemical Society (ACS). https://doi.org/10.1021/cr100290v
6. Kavadias, K. A., Apostolou, D., & Kaldellis, J. K. (2018). *Modelling and optimisation of a hydrogen-based energy storage system in an autonomous electrical network*. In Applied Energy (Vol. 227, pp. 574–586). Elsevier BV. https://doi.org/10.1016/j.apenergy.2017.08.050
7. Ma, N., Zhao, W., Wang, W., Li, X., & Zhou, H. (2024). *Large scale of green hydrogen storage: Opportunities and challenges*. In International Journal of Hydrogen Energy (Vol. 50, pp. 379–396). Elsevier BV. https://doi.org/10.1016/j.ijhydene.2023.09.021
8. Zhang, J., Zhou, Q., Tang, Y., Zhang, L., & Li, Y. (2019). *Zinc–air batteries: are they ready for prime time?* In Chemical Science (Vol. 10, Issue 39, pp. 8924–8929). Royal Society of Chemistry (RSC). https://doi.org/10.1039/c9sc04221k
9. Li, T., Huang, M., Bai, X., & Wang, Y.-X. (2023). *Metal–air batteries: A review on current status and future applications*. In Progress in Natural Science: Materials International (Vol. 33, Issue 2, pp. 151–171). Elsevier BV. https://doi.org/10.1016/j.pnsc.2023.05.007
10. Olabi, A. G., Sayed, E. T., Wilberforce, T., Jamal, A., Alami, A. H., Elsaid, K., Rahman, S. M. A., Shah, S. K., & Abdelkareem, M. A. (2021). *Metal-Air Batteries—A Review*. In Energies (Vol. 14, Issue 21, p. 7373). MDPI AG. https://doi.org/10.3390/en14217373

11. Liu, M., Lee, L. Y. S., & Wong, K.-Y. (2020). *Highly Efficient Electrocatalytic Water Splitting*. In Handbook of Nanomaterials and Nanocomposites for Energy and Environmental Applications (pp. 1–33). Springer International Publishing. https://doi.org/10.1007/978-3-030-11155-7_131-1
12. Wang, R., Chen, Z., Hu, N., Xu, C., Shen, Z., & Liu, J. (2018). *Nanocarbon-Based Electrocatalysts for Rechargeable Aqueous Li/Zn-Air Batteries*. In ChemElectroChem (Vol. 5, Issue 14, pp. 1745–1763). Wiley. https://doi.org/10.1002/celc.201800141
13. Wu, W.-F., Yan, X., & Zhan, Y. (2023). *Recent progress of electrolytes and electrocatalysts in neutral aqueous zinc-air batteries*. In Chemical Engineering Journal (Vol. 451, p. 138608). Elsevier BV. https://doi.org/10.1016/j.cej.2022.138608
14. Timofeeva, E. V., Segre, C. U., Pour, G. S., Vazquez, M., & Patawah, B. L. (2023). *Aqueous air cathodes and catalysts for metal–air batteries*. In Current Opinion in Electrochemistry (Vol. 38, p. 101246). Elsevier BV. https://doi.org/10.1016/j.coelec.2023.101246
15. Huang, Z., Wang, J., Peng, Y., Jung, C., Fisher, A., & Wang, X. (2017). *Design of Efficient Bifunctional Oxygen Reduction/Evolution Electrocatalyst: Recent Advances and Perspectives*. In Advanced Energy Materials (Vol. 7, Issue 23). Wiley. https://doi.org/10.1002/aenm.201700544
16. Ge, X., Sumboja, A., Wuu, D., An, T., Li, B., Goh, F. W. T., Hor, T. S. A., Zong, Y., & Liu, Z. (2015). *Oxygen Reduction in Alkaline Media: From Mechanisms to Recent Advances of Catalysts*. In ACS Catalysis (Vol. 5, Issue 8, pp. 4643–4667). American Chemical Society (ACS). https://doi.org/10.1021/acscatal.5b00524
17. Yang, X.-F., Wang, A., Qiao, B., Li, J., Liu, J., & Zhang, T. (2013). *Single-Atom Catalysts: A New Frontier in Heterogeneous Catalysis*. In Accounts of Chemical Research (Vol. 46, Issue 8, pp. 1740–1748). American Chemical Society (ACS). https://doi.org/10.1021/ar300361m
18. Li, J., Zhang, L., Doyle-Davis, K., Li, R., & Sun, X. (2020). *Recent advances and strategies in the stabilization of single-atom catalysts for electrochemical applications*. In Carbon Energy (Vol. 2, Issue 4, pp. 488–520). Wiley. https://doi.org/10.1002/cey2.74
19. Zhao, Y., Adiyeri Saseendran, D. P., Huang, C., Triana, C. A., Marks, W. R., Chen, H., Zhao, H., & Patzke, G. R. (2023). Oxygen Evolution/Reduction Reaction Catalysts: From In Situ Monitoring and Reaction Mechanisms to Rational Design. In Chemical Reviews (Vol. 123, Issue 9, pp. 6257–6358). American Chemical Society (ACS). https://doi.org/10.1021/acs.chemrev.2c00515

20. Lu, X., Yang, P., Wan, Y., Zhang, H., Xu, H., Xiao, L., Li, R., Li, Y., Zhang, J., & An, M. (2023). Active site engineering toward atomically dispersed M−N−C catalysts for oxygen reduction reaction. In Coordination Chemistry Reviews (Vol. 495, p. 215400). Elsevier BV. https://doi.org/10.1016/j.ccr.2023.215400
21. Kim, J., Choi, S., Cho, J., Kim, S. Y., & Jang, H. W. (2021). *Toward Multicomponent Single-Atom Catalysis for Efficient Electrochemical Energy Conversion*. In ACS Materials Au (Vol. 2, Issue 1, pp. 1–20). American Chemical Society (ACS). https://doi.org/10.1021/acsmaterialsau.1c00041
22. Yang, J., Liu, Q., Chen, S., Ding, X., Chen, Y., Cai, D., & Wang, X. (2023). *Single-Atom and Dual-Atom Electrocatalysts: Synthesis and Applications*. In ChemPlusChem (Vol. 88, Issue 10). Wiley. https://doi.org/10.1002/cplu.202300407
23. Williams, D. B., & Carter, C. B. (2009). Transmission Electron Microscopy. Springer US. https://doi.org/10.1007/978-0-387-76501-3
24. Rao, D. S., Muraleedharan, K., & Humphreys, C. J. (2010). TEM specimen preparation techniques. Microscopy: science, technology, applications and education, 2, 1232.
25. Dyck, O., Almutlaq, J., Lingerfelt, D., Swett, J. L., Oxley, M. P., Huang, B., Lupini, A. R., Englund, D., & Jesse, S. (2023). Direct imaging of electron density with a scanning transmission electron microscope. In Nature Communications (Vol. 14, Issue 1). Springer Science and Business Media LLC. https://doi.org/10.1038/s41467-023-42256-9
26. Pennycook, S. J., & Nellist, P. D. (Eds.). (2011). Scanning Transmission Electron Microscopy. Springer New York. https://doi.org/10.1007/978-1-4419-7200-2
27. Yücelen, E., Lazić, I., & Bosch, E. G. T. (2018). Phase contrast scanning transmission electron microscopy imaging of light and heavy atoms at the limit of contrast and resolution. In Scientific Reports (Vol. 8, Issue 1). Springer Science and Business Media LLC. https://doi.org/10.1038/s41598-018-20377-2
28. Skorikov, A., Batenburg, K. J., & Bals, S. (2023). Analysis of 3D elemental distribution in nanomaterials: Towards higher throughput and dose efficiency. In Journal of Microscopy (Vol. 289, Issue 3, pp. 157–163). Wiley. https://doi.org/10.1111/jmi.1316
29. Bunaciu, A. A., Udriştioiu, E. gabriela, & Aboul-Enein, H. Y. (2015). X-Ray Diffraction: Instrumentation and Applications. In Critical Reviews in Analytical Chemistry (Vol. 45, Issue 4, pp. –299). Informa UK Limited. https://doi.org/10.1080/10408347.2014.949616

30. The reflection of X-rays by crystals. (1913). In Proceedings of the Royal Society of London. Series A, Containing Papers of a Mathematical and Physical Character (Vol. 88, Issue 605, pp. 428–438). The Royal Society. https://doi.org/10.1098/rspa.1913.0040
31. Ladd, M., & Palmer, R. (2013). Structure Determination by X-ray Crystallography. Springer US. https://doi.org/10.1007/978-1-4614-3954-7
32. Fundamentals of Powder Diffraction and Structural Characterization of Materials. (2009). Springer US. https://doi.org/10.1007/978-0-387-09579-0
33. Raza, M. (2017). Oxygen vacancy stabilized zirconia (OVSZ); synthesis and properties. Unpublished. https://doi.org/10.13140/RG.2.2.30274.58566
34. Briggs, D. (1981). Handbook of X-ray Photoelectron Spectroscopy C. D. Wanger, W. M. Riggs, L. E. Davis, J. F. Moulder and G. E.Muilenberg Perkin-Elmer Corp., Physical Electronics Division, Eden Prairie, Minnesota, USA, 1979. 190 pp. $195. In Surface and Interface Analysis (Vol. 3, Issue 4). Wiley. https://doi.org/10.1002/sia.740030412
35. Wu, W., Lu, Q., Li, G., & Wang, Y. (2023). How to extract kinetic information from Tafel analysis in electrocatalysis. In The Journal of Chemical Physics (Vol. 159, Issue 22). AIP Publishing. https://doi.org/10.1063/5.0175156
36. Levich, V. G. (1962). Physiochemical hydrodynamics. Prentice-Hall.
37. Zhuang, Z., Giles, S. A., Zheng, J., Jenness, G. R., Caratzoulas, S., Vlachos, D. G., & Yan, Y. (2016). Nickel supported on nitrogen-doped carbon nanotubes as hydrogen oxidation reaction catalyst in alkaline electrolyte. In Nature Communications (Vol. 7, Issue 1). Springer Science and Business Media LLC. https://doi.org/10.1038/ncomms10141
38. Liu, Y., Dong, P., Li, M., Wu, H., Zhang, C., Han, L., & Zhang, Y. (2019). Cobalt Nanoparticles Encapsulated in Nitrogen-Doped Carbon Nanotube as Bifunctional-Catalyst for Rechargeable Zn-Air Batteries. In Frontiers in Materials (Vol. 6). Frontiers Media SA. https://doi.org/10.3389/fmats.2019.00085
39. Qin, H., Yang, Y., Shi, W., & She, Y. (2021). Heterogeneous Fenton degradation of ofloxacin catalyzed by magnetic nanostructured MnFe2O4 with different morphologies. In Environmental Science and Pollution Research (Vol. 28, Issue 21, pp. 26558–26570). Springer Science and Business Media LLC. https://doi.org/10.1007/s11356-021-12548-y
40. Sharifi, S., Rahimi, K., & Yazdani, A. (2021). Highly improved supercapacitance properties of MnFe2O4 nanoparticles by MoS2 nanosheets. In Scientific Reports (Vol. 11, Issue 1). Springer Science and Business Media LLC. https://doi.org/10.1038/s41598-021-87823-6

41. H, S. (2015). Synthesis of Carbon Nanotubes for Oil-water Interfacial Tension Reduction. In Oil & Gas Research (Vol. 1, Issue 1). OMICS Publishing Group. https://doi.org/10.4172/2472-0518.1000104
42. Aryanto, D., Sudiro, T., & Wismogroho, A. S. (2019). Correlations between Structural and Hardness of Fe-50%Al Coating Prepared by Mechanical Alloying. In PISTON: Journal of Technical Engineering (Vol. 1, Issue 2). Universitas Pamulang. https://doi.org/10.32493/pjte.v1i2.3185
43. Hjiri, M., Zahmouli, N., Khouzami, K., Mir, L. E., Aida, M. S., Moulaee, K., Lemine, O. M., Leonardi, S. G., & Neri, G. (2020). A comparison of NO2 sensing characteristics of α- and γ-iron oxide-based solid-state gas sensors. In Applied Physics A (Vol. 126, Issue 10). Springer Science and Business Media LLC. https://doi.org/10.1007/s00339-020-03829-3
44. Zhuang, L., Zhang, W., Zhao, Y., Shen, H., Lin, H., & Liang, J. (2015). Preparation and Characterization of Fe3O4 Particles with Novel Nanosheets Morphology and Magnetochromatic Property by a Modified Solvothermal Method. In Scientific Reports (Vol. 5, Issue 1). Springer Science and Business Media LLC. https://doi.org/10.1038/srep09320
45. Saputra, E., Muhammad, S., Sun, H., Ang, H.-M., Tadé, M. O., & Wang, S. (2013). Manganese oxides at different oxidation states for heterogeneous activation of peroxymonosulfate for phenol degradation in aqueous solutions. In Applied Catalysis B: Environmental (Vols. 142–143, pp. 729–735). Elsevier BV. https://doi.org/10.1016/j.apcatb.2013.06.004
46. Gao, C. Y., Baek, E., You, C. Y., & Choi, H. J. (2021). Magnetic-stimuli rheological response of soft-magnetic manganese ferrite nanoparticle suspension. In Colloid and Polymer Science (Vol. 299, Issue 5, pp. 865–872). Springer Science and Business Media LLC. https://doi.org/10.1007/s00396-021-04808-7
47. Matsoso, B. J., Ranganathan, K., Mutuma, B. K., Lerotholi, T., Jones, G., & Coville, N. J. (2016). Time-dependent evolution of the nitrogen configurations in N-doped graphene films. In RSC Advances (Vol. 6, Issue 108, pp. 106914–106920). Royal Society of Chemistry (RSC). https://doi.org/10.1039/c6ra24094a
48. Ewels, C. P., & Glerup, M. (2005). Nitrogen Doping in Carbon Nanotubes. In Journal of Nanoscience and Nanotechnology (Vol. 5, Issue 9, pp. 1345–1363). American Scientific Publishers. https://doi.org/10.1166/jnn.2005.304

49. Biesinger, M. C. (2022). Accessing the robustness of adventitious carbon for charge referencing (correction) purposes in XPS analysis: Insights from a multi-user facility data review. In Applied Surface Science (Vol. 597, p. 153681). Elsevier BV. https://doi.org/10.1016/j.apsusc.2022.153681
50. Artyushkova, K. (2020). Misconceptions in interpretation of nitrogen chemistry from x-ray photoelectron spectra. In Journal of Vacuum Science & Technology A: Vacuum, Surfaces, and Films (Vol. 38, Issue 3). American Vacuum Society. https://doi.org/10.1116/1.5135923
51. Peng, H., Mo, Z., Liao, S., Liang, H., Yang, L., Luo, F., Song, H., Zhong, Y., & Zhang, B. (2013). High Performance Fe- and N- Doped Carbon Catalyst with Graphene Structure for Oxygen Reduction. In Scientific Reports (Vol. 3, Issue 1). Springer Science and Business Media LLC. https://doi.org/10.1038/srep01765
52. Feng, J., Gao, H., Zheng, L., Chen, Z., Zeng, S., Jiang, C., Dong, H., Liu, L., Zhang, S., & Zhang, X. (2020). A Mn-N3 single-atom catalyst embedded in graphitic carbon nitride for efficient CO2 electroreduction. In Nature Communications (Vol. 11, Issue 1). Springer Science and Business Media LLC. https://doi.org/10.1038/s41467-020-18143-y
53. Biesinger, M. C., Payne, B. P., Grosvenor, A. P., Lau, L. W. M., Gerson, A. R., & Smart, R. St. C. (2011). Resolving surface chemical states in XPS analysis of first row transition metals, oxides and hydroxides: Cr, Mn, Fe, Co and Ni. In Applied Surface Science (Vol. 257, Issue 7, pp. 2717–2730). Elsevier BV. https://doi.org/10.1016/j.apsusc.2010.10.051
54. Zhang, D., Gao, J., Li, Z., He, S., & Wang, J. (2016). Synthesis of hierarchically porous carbon spheres by an emulsification-crosslinking method and their application in supercapacitors. In RSC Advances (Vol. 6, Issue 60, pp. 54880–54888). Royal Society of Chemistry (RSC). https://doi.org/10.1039/c6ra04052g
55. Chen, W., Fan, Z., Gu, L., Bao, X., & Wang, C. (2010). Enhanced capacitance of manganese oxide via confinement inside carbon nanotubes. In Chemical Communications (Vol. 46, Issue 22, p. 3905). Royal Society of Chemistry (RSC). https://doi.org/10.1039/c000517g
56. Kosmala, T., Calvillo, L., Agnoli, S., & Granozzi, G. (2018). Enhancing the Oxygen Electroreduction Activity through Electron Tunnelling: CoOxUltrathin Films on Pd(100). In ACS Catalysis (Vol. 8, Issue 3, pp. 2343–2352). American Chemical Society (ACS). https://doi.org/10.1021/acscatal.7b02690

57. Hu, J., Liu, W., Xin, C., Guo, J., Cheng, X., Wei, J., Hao, C., Zhang, G., & Shi, Y. (2021). Carbon-based single atom catalysts for tailoring the ORR pathway: a concise review. In Journal of Materials Chemistry A (Vol. 9, Issue 44, pp. 24803–24829). Royal Society of Chemistry (RSC). https://doi.org/10.1039/d1ta06144e
58. Batchelor-McAuley, C. (2023). Defining the onset potential. In Current Opinion in Electrochemistry (Vol. 37, p. 101176). Elsevier BV. https://doi.org/10.1016/j.coelec.2022.101176
59. Venkata Swetha, J., Parse, H., Kakade, B., & Geetha, A. (2018). Morphology dependent facile synthesis of manganese oxide nanostructures for oxygen reduction reaction. In Solid State Ionics (Vol. 328, pp. 1–7). Elsevier BV. https://doi.org/10.1016/j.ssi.2018.11.002
60. Zhu, Y., Zhang, B., Liu, X., Wang, D., & Su, D. S. (2014). Unravelling the Structure of Electrocatalytically Active Fe–N Complexes in Carbon for the Oxygen Reduction Reaction. In Angewandte Chemie International Edition (Vol. 53, Issue 40, pp. 10673–10677). Wiley. https://doi.org/10.1002/anie.201405314
61. Ge, X., Sumboja, A., Wuu, D., An, T., Li, B., Goh, F. W. T., Hor, T. S. A., Zong, Y., & Liu, Z. (2015). Oxygen Reduction in Alkaline Media: From Mechanisms to Recent Advances of Catalysts. In ACS Catalysis (Vol. 5, Issue 8, pp. 4643–4667). American Chemical Society (ACS). https://doi.org/10.1021/acscatal.5b00524
62. Ajmal, S., Kumar, A., Yasin, G., Alam, M. M., Selvaraj, M., Tabish, M., Mushtaq, M. A., Gupta, R. K., & Zhao, W. (2023). A microwave-assisted decoration of carbon nanotubes with Fe3O4 nanoparticles for efficient electrocatalytic oxygen reduction reaction. In Journal of Alloys and Compounds (Vol. 943, p. 169067). Elsevier BV. https://doi.org/10.1016/j.jallcom.2023.169067
63. Anantharaj, S., Karthick, K., & Kundu, S. (2017). Evolution of layered double hydroxides (LDH) as high performance water oxidation electrocatalysts: A review with insights on structure, activity and mechanism. In Materials Today Energy (Vol. 6, pp. 1–26). Elsevier BV. https://doi.org/10.1016/j.mtener.2017.07.016
64. Humayun, M., Israr, M., Khan, A., & Bououdina, M. (2023). State-of-the-art single-atom catalysts in electrocatalysis: From fundamentals to applications. In Nano Energy (Vol. 113, p. 108570). Elsevier BV. https://doi.org/10.1016/j.nanoen.2023.108570

Acknowledgments

Per prima cosa, vorrei ringraziare la mia relatrice prof. Laura Calvillo Lamana, per avermi permesso di svolgere questo lavoro di tesi e per avermi aiutato nella stesura di questo lavoro.

Grazie a tutti i membri del gruppo INCAT che mi hanno accolto con disponibilità e pazienza in una realtà per me nuova. Questi mesi trascorsi insieme saranno sempre un bel ricordo. Grazie in particolare a Nicolò, il cui contributo a questa tesi non è esplicito ma immensamente rilevante.

Grazie alla mia famiglia per avermi sostenuto in questo percorso, ascoltandomi e spronandomi nei momenti più difficili. Grazie ai miei genitori che non mi hanno mai fatto mancare niente, con lo stile però di capire cosa sia davvero necessario.

Grazie agli amici di Vittorio, indiscutibile compagnia del sabato sera. Anche se spesso siamo distanti, distratti o impegnati, quando serve ci siete sempre.

Grazie ai ragazzi del Gruppo Giovani della parrocchia di San Giacomo e ai miei colleghi animatori. Grazie per avermi insegnato che si può parlare anche di cose importanti con leggerezza, per le innumerevoli serate al Sangio ma soprattutto per la fiducia che ponete nei miei confronti.

Top-roll is for smart people